Design and Analysis of a Morphing Wing with Integrated Shape Memory Alloy Wires

A Project Report

Submitted in partial fulfilment of the

requirements for the Degree of

Master of Engineering

in

Faculty of Engineering

by

Ashok Kumar Kancharala

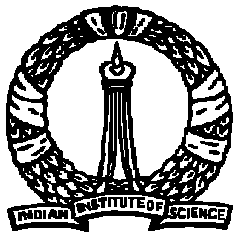

Aerospace Engineering

INDIAN INSTITUTE OF SCIENCE

BANGALORE – 560 012, INDIA

June 2008

Acknowledgements

It is a pleasure to thank many people who made this thesis possible.

It is difficult to overstate my gratitude to my guide, Dr. D Roy Mahapatra. With his enthusiasm, his inspiration, and his great efforts to explain things clearly and simply, he helped to make the work easier for me.

My sincere thanks to Dr. S. Bhaumik, NAL Bangalore for providing the SMA wire with out which the experiments would not have been a reality.

I am indebted to D. Kannan and Abhishek Wadkar for helping me doing the simulations as well as experiments. I also thank C. Sampath for fabricating the aerofoil models.

I wish to thank my friends in IISc especially from the structures lab for helping me get through the difficult times, and for all the emotional support, entertainment, and caring they provided.

I am grateful to the Chairman of the Aerospace engineering department and other teaching and non teaching staff for the helps extended in different ways.

Abstract

Finite element based simulation and sensitivity analysis of morphing aerofoil with integrated Shape Memory Alloy (SMA) wire is reported in this thesis. Experiments are carried out to validate the simulations. A coupled computational framework based on finite elements and potential flow computation is proposed to obtain the deflections of the upper and the lower skins of the aerofoil subjected to aerodynamic pressure and hysteretic deformation of the SMA wire. The computational framework couples a one-dimensional phenomenological constitutive model of SMA wire with the laminar incompressible aerodynamic pressure induced deformation of the aerofoil skins. At each step of this coupled deformation process, the deflected/morphed shape of the aerofoil is updated while computing the pressure distribution. Panel method is employed for this purpose. The aerodynamic lift is then obtained from the pressure distributions. From the simulations carried out, the optimal position and location of SMA wires are found out such that the trailing edge deflection is maximized. Changes in the aerodynamic characteristics for both stress and temperature induced transformation of SMA wires are carried out. Experiments are carried out with the estimated location and orientations while employing temperature induced transformation of SMA wire. Various aerofoil models are fabricated and experimented to maximize the trailing edge deflection. A comparison is made between simulated and the experimental results.

Contents

List of Tables

List of Figures

Chapter 1

Introduction

Different airplanes are designed to be optimal for different flight conditions. The optimal flight condition for the airplane is partially determined from the shape of the wing used. To allow for the airplane to change flight conditions during a single flight, control surfaces are incorporated into the wing design. However, these control surfaces often increase the drag on the aircraft and effectively decrease the efficiency of the aircraft. Morphing the wing would increase the efficiency of the aircraft for all flight conditions during a single mission.

Generally, aerofoils are designed for a particular flight condition and they work inefficiently at all other conditions. Therefore, the concept of morphing wing is the way forward, which can increase efficiency, manoeuvrability, and control. For example, a morphing wing would help increase the aerodynamic characteristics and control at low speeds for take off, landing and loitering of Unmanned Air Vehicles(UAVs).

1.1 Morphing Aircraft Structures: Scopes and Challenges

Morphing wing and blended wing-body are recent technologies for increasing the efficiency under multiple flight conditions during a mission. These morphing concepts have gained

tremendous attention to the aircraft industry as well as the defence R&D organisations of many developed countries [1, 2, 3]. Advances in smart materials and adaptive structures have brought promises and new ideas related to morphing aerofoils, flaps and wing shapes in order to adapt the aircraft configuration to meet all the demanding conditions. Several morphing concepts for aircraft wings have been proposed to change the chord, the span and the dihedral in order to improve the performance and control effectiveness.

Aircraft morphing concepts are being developed under two categories. One is based on multi disciplinary optimization toward passive aeroelastic tailoring of large aircraft, such as blended wing body (BWB) aircraft [6], which would take advantage of nonlinear aeroelastic regime, and the other is based on active aeroelastic tailoring using compliant structure, active linkages and electro-hydraulically enabled structures [7, 8]. There is a clear advantage of having smooth change in the shape compared to active linkage based discontinuous folding mechanisms as reported in ref. [9]. Only very recently, NASA and DARPA subcontractor in the United States (e.g., NextGen Corp. [10]) has successfully developed a prototype UAV with variable planform wing concept using truss mechanisms. The deformation of aerofoils can be achieved in two ways, one is by aerodynamics and the other is by structural means. Aerodynamic shape control uses synthetic jets to energize the flow around the aerofoil and the second approach alters the shape of the body physically, and this later aspect is closely related to the main focus of this project.
Till date, typical design objectives behind aircraft morphing components generally fall under one of the following categories:
(a) Roll control through wing warping (i.e., actuation of the aft end of the wing to achieve changes in the section camber)
(b) Wing aspect ratio changing system, forward and backward sweep to enable radical changes in wing configuration
(c) Pitching and heaving motion of wings and their coupling

Although problems under category (a) have been studied over a decade, the problems

under category (b) have become interests only recently. The problems under category (c) have new complexities [11, 12], which is because of both the strongly coupled nature of fluid-structure interaction, as well as the difficulties involved in sensor-actuator system design, control system and fatigue life etc. In this context, SMA wire based tensigrity system is the best available way forward, provided their hysterisis behaviour is characterized accurately and monitored on-line and special attention be given to adaptive control system design for their hysteritic dynamics.

Over the past few years, several successful concept realization and experiments using SMA based mechanism have been reported. Among them, notably is the development reported in [13], where a thermo-electrically controlled SMA wires packaged with air conduits were employed in a plate-array mechanism for biomimetic hydrofoil appication. Morphing aerofoil with SMA based mechanism reported in ref. [14] discusses about the change in the coefficient of pressure with a small change in the aerofoil curvature. Structural morphing, being a complex interaction between aeroelasticity and several mechanisms and or actuator dynamics, should be designed by considering the structural mechanisms, airflow, dynamics of the thin walled structure, sensors and actuators. In order to morph the surface, shape memory actuators are chosen in the present research, as they are light weight and produce large recoverable strain ($\approx 4-5\%$). For such a large strain or a large displacement, the aerofoil aerodynamics should be coupled with the thermo-mechanically induced nonlinear dynamics of the SMA wires. Stress-strain state, the location and the number of wires in the aerofoil, the amount of pre-stress in the wires and the temperature at which the wires are to be heated up are critical issues in obtaining the desired shape of the aerofoil.

1.1.1 Benefits of Morphing

The benefits of morphing are discussed in detail in the ref [4]. Variable sweep aircraft being the current state-of-the-art in shape changing wings, the next step in morphing is

to implement large changes in wing geometric parameters including sweep, span, chord and aspect ratio such changes are required to provide revolutionary improvements in system level performance. Under Phase 1 of the N-MAS program (Jan 2003, Jan 2004), the NextGen team conducted a first order study to assess the potential benefits of wing morphing. The results of this study in terms of system-level performance improvements, based on the NextGen design, are illustrated in the spider plot in Fig. 1.1.1. In this figure,

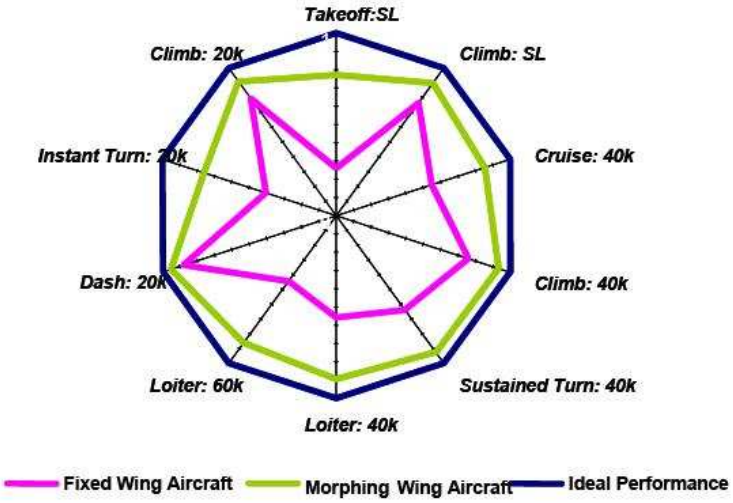

Figure 1.1: Spider plot shoeing the potential of morphing wing aircraft structure compared to fixed wing aircraft

flight performances, based on first order calculations, are shown for fixed and morphing wing geometries. The outermost points represent the theoretically best performance at each of the designated flight conditions. It should be noted that variable sweep is a subset of the NextGen design. A couple of points to note: (1) these results are based on a particular fixed-wing baseline aircraft with the morphing wing design subject to reasonable and realistic geometric constraints; and (2) while the exact values of the improved performance shown in the figure are based on text-book formulas, and are indeed indicative of potential benefits, the figure is meant to be illustrative and not definitive; they were used as a top-level justification for continued development of the technology and, as a

matter-of-fact, the entire N-MAS team found this to be sufficient rationale to proceed with the design of wind tunnel and flight models.

Mission effectiveness comparisons of Morphing and Non-Morphing vehicles is reported in detail in ref [5]. The results of studies conducted over a period of several years to determine the mission effectiveness of morphing vehicles compared to non-morphing vehicles is discussed. These studies included Killbox Interdiction and Intelligence-Surveillance-Reconnaissance scenarios with morphing vehicles, a manned fighter, and an existing UAV. The studies indicate that morphing vehicles may not always be the best performer but they are always at least good performers, which can not be said of the comparison vehicles.

1.1.2 Challenges

The main challenges of morphing a strucuture posed before are as follows.

- Integration of actuation systems,
- Optimization of system dynamics for large deformations,
- Development of a control system integrated with morphing activation and retracting mechanisms by secondary actuators, and integrated sensors for real time monitoring.
- Flight-worthiness and reliability at the stage of system-level conceptualization.

With the above research challenges in view, the development of a morphing wing is done in a systematic way. Various actuators can be used to achieve morphing of a wing and some of the actuators in use are discussed in the next section.

1.2 Actuation System Considerations

1.2.1 Actuation System Performance Requirements

In order to achieve a reasonable difference in the aerodynamic characteristics, the actuation system must generate a considerable shape change in the aerofoil. The system must fully fit within the structure of the wing and not interfere with the machining requirements of the wing or with the structural integrity of the wing. The system must be repeatable and attain the same deflection over a long run of trials. The system must also be able to hold the morphed shape safely for long periods of time without any change in the deflection. This is so that the wing can be tested for long periods of time in the wind tunnel. The actuation system must also be easily fabricated and integrated into the wing. The actuation system needs to be powered relatively easily and not require much circuitry. It should also be able to insulate itself from the rest of the wing.

1.2.2 Actuation method alternatives

In order to morph the aerofoil skins, an actuation system must be chosen. Three actuation systems were explored to morph the wing: electromagnetic, piezoelectric, and shape memory actuators. These systems were each analyzed in terms of risk, performance, and cost.

Electromagnetic actuators use solenoids to create the force to push a rod. It is this rod that is used to provide deflection for whatever purpose the actuator is being used for. The risk associated with choosing these actuators are that they are relatively large, require a fairly strong and stable material to push against since each force has an opposite and equal reaction, and they require a high power input. In terms of performance, the electromagnetic actuators produce a relatively small stroke. However, it is determined that the cost of these actuators would be relatively moderate.

Piezoelectric actuators are ceramic actuators that convert electrical energy to mechanical energy and vise versa. The performance of piezoelectric actuators would be greater than that of electromagnetic because they have a varied stroke size. However, the main risk associated with choosing piezoelectric actuators is that they require a large amount of power to operate one actuator. The smallest actuator found, weighing 1.0 gram and having dimensions of 0.88 in. x 0.38 in. x 0.021 in., would require a minimum of 480 volts peak-to-peak to deflect the material. Piezoelectric actuators are also very high in cost.

Shape memory alloy actuation was the final system explored for the morphing process. This actuation system is an alloy material that transforms to a trained shape when heated by an electrical current and returns to its original shape when cooled below the transformation temperature. These actuators apply a force as their elongation changes during transformation. The risks associated with using this actuation system are minimal. In terms of performance, the alloys can be trained to form any desired shape, they require less power to actuate, and they can generate a large force for their small size. The cost of the material is also fairly low.

Further analysis on these different actuation systems revealed that the most appropriate actuation system for the project involves the use of shape memory alloy actuators. The wires are small in size, relatively inexpensive, and can generate a large amount of force for their small size. Shape Memory Alloys (SMA) also provide the capability of customizing the deflections associated with force application by offering a variety of shapes and sizes used for actuation purposes.

SMAs, however, do have their drawbacks. They require a very large current in order to heat them to their transformation temperature quickly. They also cause problems in designing their attachment to other structures. The wire cannot not be directly soldered or epoxied to a surface; since as the wire is cycled through its transformation several times it would eventually work itself loose of these attachments. However this can be

easily overcome by the use of crimps on the ends of the wire and by lacing the wire onto the screws, which is discussed later in much further detail. They also can be easily over-heated or over-strained. This causes the repeatability of the wires to decrease to hundreds of times instead of being in the thousands. In the end the problems of SMAs were deemed to be very small compared to the problems of the other types of actuators. They were not seen as to be a risk to the success of the project and minimal compared to the problems faced using other types of actuators.
A detailed discussion of the SMA is done in the next section.

1.3 Shape Memory Alloys

The shape memory alloys (SMA) are quite fascinating materials characterized by a shape memory effect and superelasticity, which ordinary metals do not have. This unique behavior was first found in a Au-Cd alloy in 1951, and was publicized by its discover in a Ti-Ni alloy in 1963. These materials have been shown to exhibit extremely large, recoverable strains (on the order of 10). After much research and development thereafter, shape memory alloys are now being practically used in many exciting and innovative engineering applications. Furthermore, they have attracted keen attention as promising candidate for smart materials, since they function as sensors as well as actuators. These alloys can undergo martensitic phase transformations as a result of applied thermomechanical loads and are capable of recovering permanent strains when heated above a certain temperature. At high temperatures the crystal lattice is in a high symmetry, parent austenitic phase. The key characteristic of all SMAs is the occurrence of a martensitic phase transformation between the austenitic phase and the different variants of the low temperature, low symmetry martensitic phase. The martensitic transformation is a reversible shear-dominant diffusionless solid-solid phase transformation, which can be brought about by either a temperature change or by application of stress. In SMAs, this transformation can be brought about by much lower temperature change compared to conventional phase transformations like solidification that typically require large temperature change. Typical examples of shape memory alloys are Nitinol (binary alloy of Nickel and Titanium),

NiTiCu, CuAlZn and CuAlNi. Ti-Ni based shape memory alloys (SMAs) exhibit good properties in strength, ductility and resistance to corrosion, which are important for practical use, in addition to excellent SME characteristics. However they are very expensive, compared with Cu-based SMAs. Hence, inexpensive Cu-based SMAs have been investigated and developed, which have advantages in electrical and thermal conductivities and deformability compared with Ti-Ni based SMAs. Extensive literature exists that describes the SMA behavior [13 – 21].

1.3.1 Martensite transformation

The martensitic transformation (austenite- to-martensite) occurs when the free energy of martensite becomes less than the free energy of austenite at a temperature below a critical temperature T_0 at which the free energies of the two phases are equal. However, the transformation does not begin exactly at T_0 but, in the absence of stress, at a temperature Ms (martensite start), which is less than T_0. The free energy necessary for nucleation and growth is responsible for this shift [39]. The transformation continues to evolve as the temperature is lowered until a temperature, denoted by M_f (martensite finish), is reached.

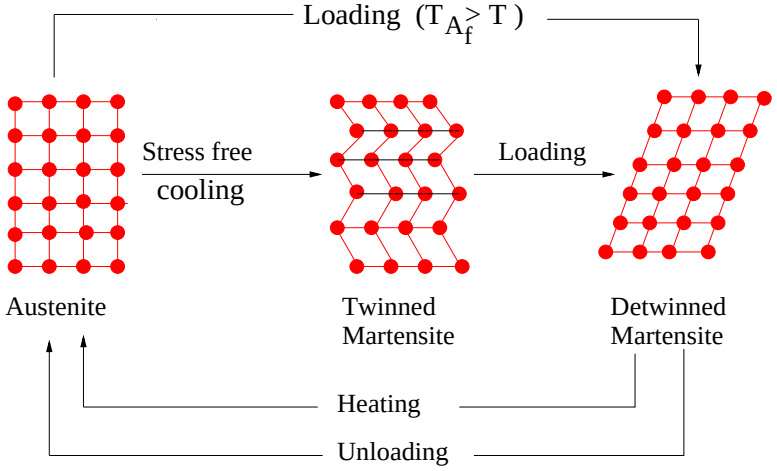

Figure 1.2: Austenite–Martensite phase transformation

When the SMA is heated from the martensitic phase in the absence of stress, the reverse transformation (martensite-to-austenite) begins at the temperature A_s (austenite start), higher than T_0. The transformation continues until a temperature A_f (austenite

finish) is reached and the material is entirely in the austenitic phase. The equilibrium temperature T_0 is approximately $(M_s + A_f)/2$ [40, 41]. When the martensitic transformation takes place, numerous physical properties are modified. During the transformation, a latent heat associated with the transformation is absorbed or released based on the transformation direction. The forward, austenite- to-martensite ($A \rightarrow M$) transformation is accompanied by the release of heat corresponding to a change in the transformation enthalpy (exothermic phase transformation). The reverse, martensite-to-austenite ($M \rightarrow A$) transformation is an endothermic phase transformation accompanied by absorption of thermal energy. For a given temperature, the amount of heat is proportional to the volume fraction of the transformed material. Summarized below are the main characteristics of martensitic phase transformations that distinguish them among other solid-state transformations: (1) It is associated with an inelastic deformation of the crystal lattice with no diffusive process involved. It results from a cooperative and collective motion of atoms over distances smaller than the lattice parameters. The absence of diffusion makes the martensitic phase transformation almost instantaneous [42]. (2) Parent and product phases coexist during the phase transformation, since it is a first order transition, and as a result there exists an invariant plane, which separates the parent and product phases. (3) Transformation of a unit cell element produces a volumetric and a shear strain along well defined planes. The shear strain is many times larger than the elastic distortion of the unit cell. This transformation is crystallographically reversible [43]. (4) Since the crystal lattice of the martensitic phase has lower symmetry than that of the parent austenitic phase, several variants of martensite can be formed from the same parent phase crystal [44]. (5) Stress and temperature have a large influence on the martensitic transformation. Transformation takes place when the free energy difference between the two phases reaches a critical value [39].

Martensitic transformations are usually divided into two groups − thermoelastic and non-thermoelastic. The non-thermoelastic transformations occur mainly in ferrous alloys and are associated with non-mobile martensite-parent phase interfaces pinned by permanent defects and proceed by successive nucleation and growth. Due to re-nucleation of

austenite during the reverse (martensite to austenite) transformation, these transformations are crystallographically non-reversible in the sense that the martensite cannot revert to the parent phase in the original orientation. The thermoelastic martensitic transformations, on the other hand, are associated with mobile interfaces between the parent and martensitic phases. These interfaces are capable of backward movement during the reverse transformation by shrinkage of the martensitic plates rather than nucleation of the parent phase, which leads to a crystallographically reversible transformation [41]. The unique properties of SMAs (i.e., shape memory effect, pseudoelasticity) are the result of thermoelastic martensitic transformation.

1.3.2 Shape Memory Effect

Shape memory effect is exhibited when the SMA is deformed while in the martensitic phase and then unloaded while still at a temperature below M_f. When subsequently heated above A_f, it regains its original shape by transforming back into the austenitic phase. A typical loading path $1 \rightarrow 2 \rightarrow 3 \rightarrow 4 \rightarrow 1$, in which the SME is observed, schematically plotted in stress−strain−temperature space is shown in Fig. 1.3.2 During the cooling of the parent phase ($1 \rightarrow 2$) it transforms to twinned martensite. The material is then loaded ($2 \rightarrow 3$) causing stress induced detwinning and development of inelastic strains. Upon unloading ($3 \rightarrow 4$) the material remains in detwinned state and the inelastic strains are not recovered. Finally, when it is heated above A_f ($4 \rightarrow 1$), the SMA returns to its cubic parent phase and the inelastic strains are recovered. The crystallographic changes during this loading path are explained next. The stress-free cooling of austenite produces self-accommodating growth of the martensitic variants ($1 \rightarrow 2$) such that there is no macroscopic transformation strain [45]. The self-accommodated morphology is a characteristic of the crystallography of the alloy used. For example, in copper-based alloys, 24 variants of martensite constitute six self-accommodated groups. The growth of such groups produces no macroscopic transformation strain, but the multiple interfaces present in these structures (boundaries between the martensite variants and twinning interfaces) are very mobile. This great mobility is at the heart of the shape memory

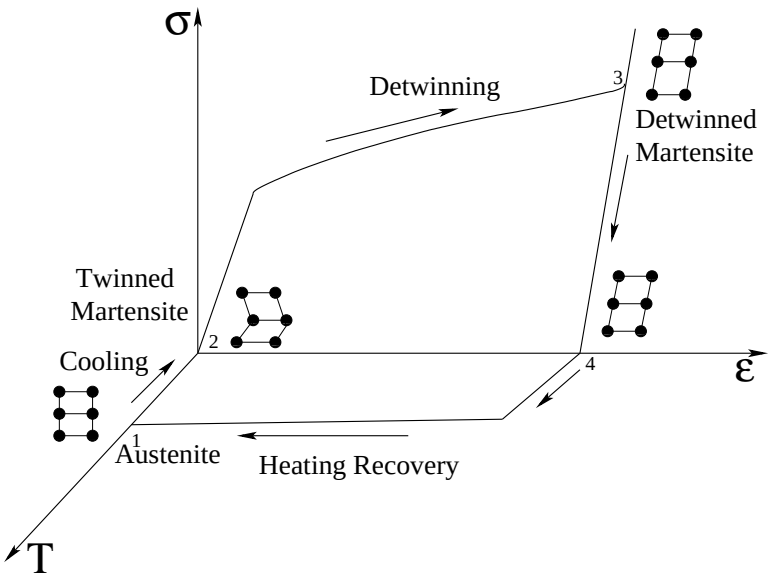

Figure 1.3: Stress-strain-temperature schematic of the crystallographic changes involved in the shape memory effect.

effect. Movement of these interfaces accompanied by detwinning is obtained at stress levels far lower than the plastic yield limit of martensite. This mode of deformation, called reorientation of variants, dominates at temperatures lower than M_f. During the second stage ($2 \rightarrow 3$), the mechanical loading in the martensitic phase leads to reorientation of the variants and results in development of large inelastic strains. This inelastic strain is not recovered upon unloading ($3 \rightarrow 4$). During the last step ($4 \rightarrow 1$), heating the sample above A_f induces the reverse transformation and recovers the inelastic strain. When the temperature approaches A_f, the martensitic phase becomes unstable in the absence of stress. This results in a complete transformation to the parent phase. Since martensite variants have been reoriented by stress, the reversion to austenite produces a large transformation strain having the same amplitude but opposite direction to the inelastic strain. As a result, the SMA returns to the original shape it had in the austenitic phase.

1.3.3 Pseudoelasticity

The pseudoelastic behavior of SMAs is associated with stress induced strain recovery upon unloading at temperatures above A_f. Under most general conditions, pseudoelastic thermomechanical loading paths start at zero stress in the austenitic region, then move to the detwinned martensite region and then unload again to the starting point. An example is the path $a \rightarrow b \rightarrow c \rightarrow d \rightarrow e \rightarrow a$ shown on Fig. 1.3.3. We consider the thermomechan-

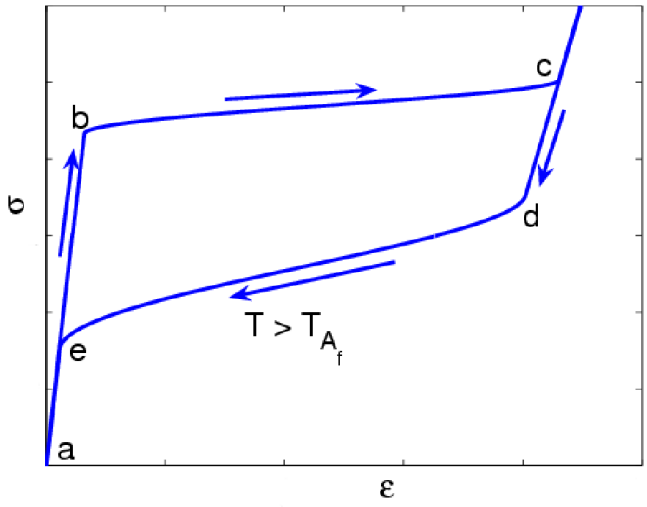

Figure 1.4: $\sigma - \epsilon$ plot depicting Pseudoelasticity.

ical loading path $a \rightarrow b \rightarrow c \rightarrow d \rightarrow e \rightarrow a$, which starts at zero stress level, above A_f. When the material is loaded at temperatures above A_f, the parent phase (austenite) undergoes thermoelastic loading up to a critical stress level called the Transformation stress $(a \rightarrow b)$. At this stress level the material undergoes a stress induced phase transformation $(b \rightarrow c)$ from austenite to martensite during which large inelastic strains are developed. Any subsequent loading in the detwinned martensitic region $(c \rightarrow d)$ does not produce further phase transformation, although reorientation of the martensitic twins may occur in multiaxial loading conditions. When the point (d) is reached, the reverse transformation begins (martensite- to-austenite), leading to recovery of the inelastic strains. The material

fully transforms to austenite at (e) and the final segment of the loading path ($e \rightarrow a$) is characterized by recovery of the thermoelastic strains, leading to zero macroscopic strains upon completion of the path. The transformation process results in a hysteresis, which reflects the energy, dissipated in the cycle. A literature survey has been done on the SMA actuator systems which is discussed in the next section.

1.4 Literature Survey

In the recent years, a lot of work is being done on the application of SMA actuators for various purposes. The techniques developed by various people in the application of these actuators for various problems are outlined in this section.

1.4.1 Shape Memory Alloy Wire Actuators

The shape memory alloy wires are used as actuators as they have the capability of applying stress on the structures when the temperature or the stress of the material is varied. SMA actuators have been developed to act as muscles for an ambulatory robot modeled after the American lobster [15]. Each muscle consists of a 250μ diameter Nitinol wire. The ends of the each wire are formed into a small loop using a metal crimp. Much like the muscles work in the natural organisms, the Nitinol wires are used in antagonistic pairs. To contract the muscle, current pulses are sent through the wire.

An SMA actuated biomimetic hydrofoil was developed by Rediniotis [13, 16]. In this application, the SMA actuators were also used to mimic muscles. However a different technique was used. Instead of using two antagonistic SMA wires, a bias spring is used to provide the restoring force for the SMA wire. Each SMA wire was attached to the skin of the hydrofoil using a Kevlar tendon. By actively controlling the temperature of the SMA wire, actuation frequencies up to 20 hertz were achieved. This is a ground breaking research as actuation frequencies of this magnitude are commonly thought to be unobtainable when using SMA actuators.

Strelec and Lagoudas [14] fabricated and tested an SMA actuated wing which used two-way trained SMA wires. Heating and cooling were done through resistive heating and natural convection, respectively. This discusses about the change in the coefficient of pressure with a small change in the aerofoil curvature.

1.4.2 Large Scale SMA Wire Actuators

The DARPA Smart wing program has investigated the use of SMA torque tubes to induce wing warping in a full scale aircraft wing [17, 18]. This torque tube is designed to replace electric or hydraulic torsion actuators. The stiffness of the wing box is used to provide the restoring force to the torque tube, which is pre-strained before it is installed.

An important difference between this concept and those using SMA wire is the method of heating the actuator. Unlike in the wire actuators, direct resistive heating was found to be inefficient in terms of both uniformity of heating and power consumption. For this reason, heat was added by wrapping the torque tube in heater wire. In terms of aerodynamic performance, this program has shown that SMA actuation can provide wing twist sufficient to create the roll moments needed to control the aircraft. Additionally, this study has shown that the use of hingeless control surfaces increases lift and decreases drag by delaying the flow separation of the wing.

1.4.3 Shape Memory Alloy Composites

Several efforts have been made to embed SMA's in composites to investigate the properties of SMA's to control the beam dynamics or other structures. Liang, Jia and Rogers investigated embedding Nitinol wires in a graphite/epoxy composite beam to control vibration and alter natural frequencies [19, 20]. Resistive heating was used to trigger a phase change in the wires. In order to build the SMA composite beams, pre-strained

wires are included in the initial lay-up,and they were constrained to prevent them from changing shape during the curing process. Various methods are discussed to control the vibration of the beam.

Several authors discussed the usage of SMA wire embedded composites to control the vibration of the structures [21, 22, 23]. Several other studies have been completed to optimize the actual process of producing SMA coposites. The utilization of two-way shape memory effect to overcome the problems with the resulting bond between the SMA wires and the surrounding epoxy is discussed in ref [24, 25]. The structural deformation that can be obtained using embedded SMA wires is analyzed in ref [26, 27]. Morphing an airfoil section using composite structures is investigated in ref. [28, 29].

1.5 Objective of thesis

The main objective of this project is to develop a morphing aircraft structure based on a specific design concept, namely, Shape Memory Alloy (SMA) wire elements and actively controlled mechanism integrated with in a simple aerofoil for morphing. Here, the notion of morphing is restricted by the fact that only the aerofoil shape change (including the trailing edge deflection) will be engineered. Another objective is to quantify the aerodynamic coefficients under steady flow to emphasize the concept of morphing technology.

Attempts have been made by several researchers to achieve morphing using compliant mechanisms, active linkages and smart structures, but they had a limited success with the coupled analysis of SMA wire hysteritic dynamics and fluid-structure interaction. Finite element based simulation and sensitivity analysis of morphing aerofoil with integrated Shape Memory Alloy (SMA) wire is reported in this thesis. From from the simulations carried out, the optimal position and location of SMA wires is found out to maximize the trailing edge deflection along with the change in the aerodynamic characteristics for both Stress and temperature induced transformation of SMA wires. Also, a comparison of simulated and experimental results is reported.

To define the project objectives in more detail, there are several objectives that are considered in order to meet the overall project objective. they are listed below.

- To develop a morphing aircraft structure based on a specific design concept, namely, Shape Memory Alloy (SMA) wire elements and actively controlled mechanism integrated with in a simple aerofoil for morphing.
- Finite element based simulation and sensitivity analysis of morphing aerofoil with integrated Shape Memory Alloy (SMA) wire
- Definition of an effective actuation system, which would initiate and control the shape change of the wing.
- Definition of a structural and material system that allows the wing to remain structurally sound, compromising the flexibility necessary to morph the shape of the wing and the stiffness required to ensure structural integrity.
- Development of an electrical circuit for the actuation of SMA wire.
- Verification of the aerodynamic performance of the morphing wing.

1.6 Overview

The plan of this thesis is as follows: Chapter 2 provides the details of the preliminary design carried out to estimate the range of parameters.Chapter 3 describes the developed model for the coupled analysis. This chapter focuses on the constitutive model proposed by Brinson(1993), a 2-D inviscid,incompressible flow panel method in brief and the detailed formulation of coupled finite elements of SMA wire integrated aerofoil. This chapter also presents the analysis carried out to find out optimum position and location of SMA wire with in the aerofoil to achieve maximum trailing edge deflection. In chapter 4, discussion about various fabricated aerofoils and their experimental results is reported. Chapter 5 provides future scope of research and conclusions.

Chapter 2

Preliminary Design

The main focus of this project is on the realization of an active morphing concept based on the SMA wire and the compliant structure integrated with in an aerofoil. To achieve a smooth and considerable change in the shape of the wing, it is divided into a number of segments and SMA wires are used to deflect each segment seperately.Each segment consists of an actuation system and finally all the segments are joined to form a complete wing.

A preliminary design has been carried out to find out the number of segments and the range of parameters has been estimated. The aerofoil span is divided into a number of segments and each segment is attached with SMA wires, while keeping in mind that the structural stability and stiffness against bending and pitching are important. The wires are attached to the top and the bottom surfaces of the skin perpendicular to the horizontal stiffener plate. The segments of aerofoils are arranged in the span-wise direction using slotted arrangement. The number and span of the segments are calculated based on the lift and the force exerted by the SMA wires on the skin.

For preliminary analysis, a symmetric aerofoil (NACA0021) is considered as it can be fabricated easily and also the variation in the thickness will be prominent with the actuation of SMA wires. At present, we restrict ourselves to the free stream velocity range of $15 - 40$ m/s. By assuming the air density (ρ)=$1.225 kg/m^3$, dynamic fluid viscosity

(μ)=$1.85 \times 10^{-5} N - s/m^2$ at 25^0C, and 1 bar free-stream pressure, free-stream velocity of 40 m/s, the Reynolds number is found to be

$$Re = \rho V l/\mu = 8X10^5, \tag{2.1}$$

Considering a chord length of 1ft for a NACA0021 aerofoil as the reference aerofoil, the coefficients of lift, drag and pitching moment are found to be

$$C_L = 0.4998, \quad C_D = 0.0129, \quad C_M = 0,$$

The above estimates are for 5^0 angle of attack and $Re = 8$ X 10^5. Assuming the aerofoil span to be 3ft, the total surface area of the plan form becomes $S = 0.2787m^2$. The aerodynamic lift force on the aerofoil is then

$$L = \frac{1}{2}\rho_\infty {V_\infty}^2 S C_L = 136.50N, \tag{2.2}$$

the aerodynamic drag is

$$D = \frac{1}{2}\rho_\infty {V_\infty}^2 S C_D = 3.5N, \tag{2.3}$$

and the pitching moment $M = 0$. Assuming the SMA wire diameter $d = 0.5$ mm, and the force acting on the SMA wire is $8N$, one has Number of span-wise segments of aerofoil = total lift force / (force on each aerofoil segment)

$$\frac{136.5}{8} = 18, \tag{2.4}$$

Span of each segment is then approximately 5cm.

This preliminary design is helpful in carrying out the simulations and to fabricate the aerofoil model. A NACA aerofoil of 30.48 cm chord length and 5 cm width is used for the simulations that are carried out in the next section. Aerofoil models are fabricated with the same dimensions and tested.

Chapter 3

Modeling and Simulation

In this section, a computational model is formulated along with the one-dimensional constitutive model of SMA wire. Next, various issues in coupling a pressure based code using panel method with the finite element model of the morphing aerofoil is discussed.
The stress-strain behaviour of SMA wire is characterized using a 1-D constitutive model and this is used in the coupled computational model to obtain the force exerted by the SMA wire on the aerofoil. The various criteria required for the transformation are discussed in detail in Sec. 3.1.
Finite element analysis of the coupled SMA-aeroelastic problem is formulated from the first principles. The governing differential equations of the aerofoil are coupled with the constitutive model of SMA wire and the solution is obtained on the finite element basis. The detailed discussion regarding this analysis is given in Sec. 3.2.
The aerodynamic pressure acting on the aerofoil is calculated using the 2-D panel method and the force exerted by this pressure is applied on the aerofoil in a finite element sense. A brief discussion of the panel method used is given in Sec. 3.3

3.1 One-dimensional model of SMA wire

The behavior of the material is primarily a function of three variables: stress, strain and temperature, and their associated rates. These variables are interdepen- dent, and the

material behavior is a nonlinear function of these variables involved. A constitutive model attempts to describe the material behavior as a function of these variables. These models are based on thermo- mechanics, or a combination of thermomechanics and SMA phenomenology. The properties of a particular alloy depend on the precise composition of the constituent materials, the processing technique and other factors involving the manufacturing and heat treatment of the alloy. To accommodate these varia- tions, most of these constitutive models employ specific material parameters that are determined by experimen- tation for a particular material. Most of these constitu- tive models are developed for quasistatic loading only, and it is assumed that the material at each instant is in thermodynamic equilibrium.

One of the first constitutive models, developed by Tanaka in 1986, is based on thermomechanics. In this model, the second law of thermodynamics was written in terms of the Helmholtz free energy. It was assumed that unidirectional strain, temperature and martensite volume fraction are the only state variables, and the stress is calculated as a function of these variables. It may be noted that the martensitic volume fraction is a function of the stress and temperature, making a recursive numerical solution necessary in order to determine both stress and volume fraction simulta- neously. The transformation kinetics are described by an exponential expression to describe the martensite volume fraction as a function of stress and temperature.

Liang and Rogers (1990) formulated a model based on the rate form of the constitutive equation developed by Tanaka. In constrast to Tanakas model, however, a cosine model was developed to characterize the marten- sitic volume fraction.

A major drawback of the Tanaka, and Liang and Rogers models in their original form is that they only describe the phase transformation from martensite to austenite and vice versa, and cannot be applied to model the detwinning of martensite that is responsible for the shape memory effect at lower temperatures. Thus, they cannot describe the actuation behavior with strain recovery effectively.

In order to distinguish between the various forms of martensite, the martensite volume fraction was separated into two parts by Brinson and coworkers (Brinson, 1990).

The stress-induced martensitic volume fraction describes the amount of detwinned or stress- preferred variant of martensite present in the sample, and the temperature-induced martensite describes the fraction of martensite (containing all variants) that occurs from the reversible phase transformation with austenite. The coefficients of the constitutive equation are assumed to be nonconstant in order to account for both the shape memory and pseudoelasticity effects.

From the above discussion, it is clear that the Brinson's constitutive model captures the behaviour of SMA better than the other models and so this model is chosen for the analysis in the present work.

Brinson's constitutive model [46] along with the necessary modification [47] satisfying certain consistency requirements is implemented in the present study for characterizing the stress-strain behaviour of the constrained SMA wire. The constitutive model is given by

$$\sigma - \sigma_o = D(\xi)\epsilon - D(\xi_o)\epsilon_o - \epsilon_l D(\xi_o)\xi_{so} + \Theta(T - T_o) \tag{3.1}$$

where σ is the stress, ϵ is the total strain, D is the stiffness coefficient, ϵ_l is the maximum residual strain (volume averaged transformation strain), ξ is the martensitic volume fraction, Θ is the thermal coefficient of expansion, T is the temperature and the variables with subscript 0 indicate initial values. The total martensite volume fraction (ξ) can be resolved into stress-induced part (ξ_S) and a temperature-induced part (ξ_T) as

$$\xi = \xi_S + \xi_T \tag{3.2}$$

For the transformation of austenite to detwinned martensite, the following set of conditions are introduced.

For $T > A_S$ and $(\sigma_s{}^{cr} + C_M(T - M_s)) < \sigma < (\sigma_f{}^{cr}) + C_M(T - M_s))$

$$\xi_s = \frac{1 - \xi_{so}}{2}\cos[\frac{\pi}{\sigma_s{}^{cr} - \sigma_f{}^{cr}}(\sigma - \sigma_f{}^{cr} - C_M(T - M_s))] + \frac{1 + \xi_{so}}{2}$$

$$\xi_T = \xi_{T_o} - \frac{\xi_{T_o}}{1 - \xi_{S_o}}(\xi_S - \xi_{S_o})$$

For $T < M_s$ and ${\sigma_s}^{cr} < \sigma < {\sigma_f}^{cr}$

$$\xi_s = \frac{1-\xi_{so}}{2}\cos[\frac{\pi}{{\sigma_s}^{cr} - {\sigma_f}^{cr}}](\sigma - {\sigma_f}^{cr}) + \frac{1+\xi_{so}}{2}$$

$$\xi_T = \xi_{T_o} - \frac{\xi_{T_o}}{1-\xi_{S_o}}(\xi_S - \xi_{S_o}) + \Delta T_\epsilon$$

where if $M_f < T < M_s$ and $T < T_o$

$$\Delta T_\epsilon = \frac{1-\xi_{T_o}}{2}\cos(a_M(T - M_f) + 1)$$

else $\Delta T_\epsilon = 0$

For transformation of martensite to austenite, the phase fraction variables are defined as follows.

For $T > A_s$ and $C_A(T - M_f) < \sigma < C_A(T - A_s)$

$$\xi = \frac{\xi_o}{2}\cos(a_A(T - A_s - \frac{\sigma}{C_A}) + 1)$$

$$\xi_S = \xi_{S_o} - \frac{\xi_{S_o}}{\xi_o}(\xi_o - \xi)$$

$$\xi_T = \xi_{T_o} - \frac{\xi_{T_o}}{\xi_o}(\xi_o - \xi) \tag{3.3}$$

where A_s is the austenite start temperature, A_f is the austenite finish temperature, M_s is the martenite start temperature, M_f is the martenite finish temperature, ${\sigma_s}^{cr}$ and ${\sigma_f}^{cr}$ are the critical transformation stresses. Above the value of M_s, the critical transformation stress is a function of temperature. The slope of these transformation phase boundaries in the σ-T space is given by C_M and C_A as shown in Fig. 3.1. a_M and a_A are defined by

$$a_M = \frac{\pi}{(M_s - M_f)}\ , \quad a_A = \frac{\pi}{(A_f - A_s)}$$

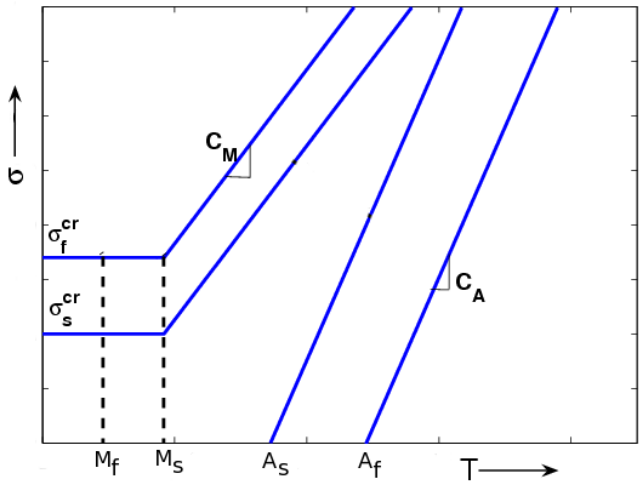

Figure 3.1: Phase diagram (Brinson, 1993).

The constitutive model discussed here is used to obtain the actuation force of SMA wire acting on the aerofoil. The solution to this non-linear model is obtained on a finite element basis as described in the next section. The stress-strain-temperature relationships discussed are used to obtain the actuation force in a hysteritic manner.

3.2 Finite Element modeling of SMA integrated aerofoil

A NACA0021 aerofoil is considered for vertical positioning and NACA4421 for the angular positioning of SMA wires for the present analysis and experiments. Fig. 3.2 shows a schematic diagram of the SMA wire-skin element subjected to aerodynamic pressure distribution P(x) and force (F) due to SMA actuator ends connected to both the skins of the aerofoil. The aerofoil skins are constrained by the leading edge and the trailing edge stiffeners. Therefore, our analysis is restricted to the skin parts excluding the stiffener members, that is, between the region x_1 and x_2 as shown in Fig. 3.2. As the forces acting are not same on the entire aerofoil, it is divided into two regions A and B representing the upper and lower skins respectively, and the SMA wire region is denoted by C. The

deflections of the surfaces are obtained by considering the Euler-Bernoulli beam kinematics and by solving the coupled differential equations for arbitrary curved segments. The

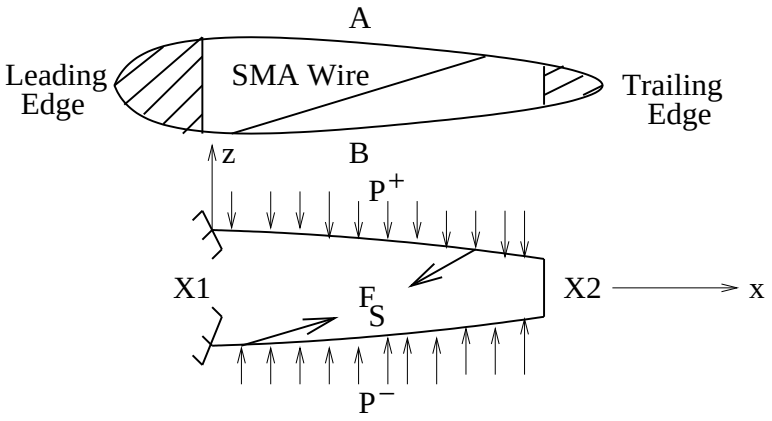

Figure 3.2: Schematic diagram showing the SMA wire and the skin elements.

thickness distribution for a NACA 4 digit aerofoil is given by

$$Z = \pm\frac{t}{0.2}(0.2969\sqrt{x} - 0.1260x - 0.3516x^2 + 0.2843x^3 - 0.1015x^4) \tag{3.4}$$

where t is the maximum thickness of the aerofoil and x is the chord axis.
The wing is divided in to a number of segments and each segment is modeled as a beam using the Euler-Bernoulli beam kinematics expressed as

$$u = u_0(x) - z\frac{\partial w}{\partial x}, \quad w = w(x) \tag{3.5}$$

where u is the differential axial displacement, u_o is the pure axial displacement, $z\frac{\partial w}{\partial x}$ is the axial displacement due to bending and w is the transverse displacement. Applying Hamilton's first principle, one has

$$\delta\int_0^t (U - T + W)dt = 0 \tag{3.6}$$

where U is the strain energy, T is the kinetic energy and W is the external work done; that is

$$U = \int \frac{1}{2}\sigma^T \epsilon d\Omega, \quad T = \int \frac{1}{2}\rho(\dot{u}^2 + \dot{w}^2)d\Omega, \quad W = \sum_{i=0}^{L} f_u u_i + \sum_{i=0}^{L} f_w w_i \tag{3.7}$$

where ρ is the density of the aluminium, f_u and f_w are the forces acting on the aerofoil due to aerodynamic pressure and the SMA wire actuator applied as point loads at the nodes. u_i and w_i are the corresponding displacements at the node 'i'. The governing differential equations and the boundary conditions are obtained using the Hamilton's principle in Eq. 3.6, which are expressed as

$$\delta u_0 : \quad \rho A\ddot{u}_0 - EA\frac{\partial^2 u_0}{\partial x^2} + EA_1\frac{\partial^3 w}{\partial x^3} - \rho A_1\frac{\partial \ddot{w}}{\partial x} + f_u = 0 \tag{3.8}$$

$$\delta w : \quad \rho A\ddot{w} - EA_1\frac{\partial^3 u_0}{\partial x^3} + EI\frac{\partial^4 w}{\partial x^4} + \rho A_1\frac{\partial \ddot{u}_0}{\partial x} - \rho I\frac{\partial^2 \ddot{w}}{\partial x^2} + f_w = 0 \tag{3.9}$$

where f_u and f_w denote the forces acting through out the body in longitudinal and transverse directions respectively. Neglecting the inertia terms for this problem, the governing differential equations for the upper and lower skins are expressed as

$$EA\frac{\partial^2 u_{0_A}(x)}{\partial x^2} - EA_1\frac{\partial^3 w_A(x)}{\partial x^3} = f_{u_A} \tag{3.10}$$

$$EI\frac{\partial^4 w_A(x)}{\partial x^4} - EA_1\frac{\partial^3 u_{0_A}(x)}{\partial x^3} = -P^+ \tag{3.11}$$

$$EA\frac{\partial^2 u_{0_B}(x)}{\partial x^2} - EA_1\frac{\partial^3 w_B(x)}{\partial x^3} = f_{u_B} \tag{3.12}$$

$$EI\frac{\partial^4 w_B(x)}{\partial x^4} - EA_1\frac{\partial^3 u_{0_B}(x)}{\partial x^3} = -P^- \tag{3.13}$$

where

$$A = bh, \quad A_1 = \frac{bh^2}{4}, \quad I = \frac{bh^3}{12},$$

E is the Young's modulus, h is the thickness of the aerofoil skin, b is the span of the aerofoil, f_{u_A} and f_{u_B} denote the forces acting through out the body in longitudinal direction

on upper and lower skins respectively, P^+ and P^- are the aerodynamic pressures acting on the upper and lower skins respectively.

The Governing differential equation of the SMA wire obtained from one-dimensional constitutive equation is given by

$$\frac{\partial \sigma(\xi, T, \epsilon)}{\partial z'} = \frac{\partial}{\partial z'}[(D(\xi)\epsilon - D(\xi_o)\epsilon_o - \epsilon_l D(\xi_o)\xi_{so} + \Theta(T - T_o))] = 0 \tag{3.14}$$

with boundary conditions $\sigma A_{SMA} = \pm F_S$.

where A_{SMA} is the cross-sectional area of the SMA wire, F_S is the force (see Fig 3.2) and $z' = (L - f(u, w))$ is the instantaneous length of the SMA wire due to combined effect of the deflections of the top and bottom skins. The weak solution of the above system of coupled nonlinear partial differential equations (Eqs. (3.10)– (3.14)) is obtained by writing the following weighted residual form

$$\begin{aligned}
&\int \quad \delta\bar{u}_A[EA\frac{\partial^2 u_{0_A}(x)}{\partial x^2} - EA_1\frac{\partial^3 w_A(x)}{\partial x^3} - f_{u_A}]dS_A \\
&+ \quad \int \delta\bar{w}_A[EI\frac{\partial^4 w_A(x)}{\partial x^4} - EA_1\frac{\partial^3 u_{0_A}(x)}{\partial x^3} + P^+]dS_A \\
&+ \quad \int \delta\bar{u}_B[EA\frac{\partial^2 u_{0_B}(x)}{\partial x^2} - EA_1\frac{\partial^3 w_B(x)}{\partial x^3} - f_{u_B}]dS_B \\
&+ \quad \int \delta\bar{w}_B[EI\frac{\partial^4 w_B(x)}{\partial x^4} - EA_1\frac{\partial^3 u_{0_B}(x)}{\partial x^3} + P^-]dS_B \\
&+ \quad \int \delta\bar{u}_S[\frac{\partial \sigma(\xi, T, \epsilon)}{\partial z}]d\Omega_E = 0
\end{aligned} \tag{3.15}$$

where $dS_A = \sqrt{1 + (dZ_A/dx)^2}dx = \lambda_A dx$, $dS_B = \sqrt{1 + (dZ_B/dx)^2}dx = \lambda_B dx$ and the quantities with overhead bar $(\bar{u}_A, \bar{w}_A, \bar{u}_B, \bar{w}_B, \bar{u}_S)$ are the weight functions from the space of admissible functions which minimize the total energy of the system. Z is the thickness distribution of the aerofoil (refer Eq. 3.4) and the subscripts A and B represent the quantities related to upper and lower skins of the aerofoil respectively. The displacement interpolation functions are approximated as

$$\bar{u} = N_u \bar{u}^*, \quad \frac{\partial \bar{u}}{\partial x} = D_u \bar{u}^*$$

$$u_0 = N_u {u_0}^*, \quad \frac{\partial u_0}{\partial x} = D_u {u_0}^*$$

$$\bar{w} = N_w \bar{w}^*, \quad \frac{\partial \bar{w}}{\partial x} = D_w \bar{w}^*, \quad \frac{\partial^2 \bar{w}}{\partial x^2} = B_w \bar{w}^*$$

$$w = N_w w^*, \quad \frac{\partial w}{\partial x} = D_w w^*, \quad \frac{\partial^2 w}{\partial x^2} = B_w w^*$$

where N_u is the Lagrangian shape function to approximate the longitudinal displacement, $D_u = \partial \bar{N}_u / \partial x$, N_w is the Hermitian shape function to approximate the transverse displacement, $D_w = \partial \bar{N}_w / \partial x$, $B_w = \partial^2 \bar{N}_w / \partial x^2$ and the quantities with superscript '$*$' are the nodal displacements.

The finite element system equation is finally obtained by integrating Eq. (3.15) by parts and it is written in the matrix-vector form as

$$\begin{bmatrix} K_{AA} & K_{AB} & K_{AS} \\ K_{BA} & K_{BB} & K_{BS} \\ K_{SA} & K_{SB} & K_{SS} \end{bmatrix} \left\{ \begin{Bmatrix} u_A \\ w_A \end{Bmatrix} \begin{Bmatrix} u_B \\ w_B \end{Bmatrix} \begin{Bmatrix} u_s \\ w_s \end{Bmatrix} \right\} = \begin{Bmatrix} F_A \\ F_B \\ F_S \end{Bmatrix} \tag{3.16}$$

where $\{u\}^e = \{u_A \quad w_A \quad u_B \quad w_B \quad u_S \quad w_S\}^T$denotes the nodal displacement sub-vectors consisting of degrees of freedom for the top skin (A), the bottom skin (B) and the SMA wire (S).

K_{AA} and K_{BB} are the elemental stiffness matrices of the upper and lower skins of the aerofoil. K_{AB} and K_{BA} represent the stiffness of the elements connected to both the upper and lower skins (trailing edge in this case). K_{AS}, K_{SA}, K_{BS} and K_{SB} represent the stiffness of the elements of the SMA wire connected to either the upper or the lower skin. K_{SS} is the elemental stiffness matrix of the SMA wire.

The elemnts of the stiffness matrix are obtained as

$$\begin{aligned}
K_{AA} = \; & - \int {N_u}^T EAD_u\lambda_A{}'dx - \int {D_u}^T EAD_u\lambda_A{}'dx + \int {N_u}^T EA_1B_w\lambda_A{}'dx \\
& + \int {D_u}^T EA_1B_w\lambda_A dx + 2\int {D_w}^T EIB_w\lambda_A{}'dx + \int {N_w}^T EIB_w\lambda_A{}''dx \\
& + \int {B_w}^T EIB_w\lambda_A dx - 2\int {D_w}^T EA_1D_u\lambda_A{}'dx - \int {N_w}^T EA_1D_u\lambda_A{}''dx \\
& - \int {B_w}^T EA_1D_u\lambda_A dx, \\
K_{BB} = \; & - \int {N_u}^T EAD_u\lambda_B{}'dx - \int {D_u}^T EAD_u\lambda_B{}'dx + \int {N_u}^T EA_1B_w\lambda_B{}'dx \\
& + \int {D_u}^T EA_1B_w\lambda_B dx + 2\int {D_w}^T EIB_w\lambda_B{}'dx + \int {N_w}^T EIB_w\lambda_B{}''dx \\
& + \int {B_w}^T EIB_w\lambda_B dx - 2\int {D_w}^T EA_1D_u\lambda_B{}'dx - \int {N_w}^T EA_1D_u\lambda_B{}''dx \\
& - \int {B_w}^T EA_1D_u\lambda_B dx,
\end{aligned}$$

where

$$\lambda' = \frac{\partial\lambda}{\partial x}, \lambda'' = \frac{\partial^2\lambda}{\partial x^2},$$

$$\begin{aligned}
K_{AB} &= K_{BA}, \\
K_{AS} &= K_{BS} = K_{SA} = K_{SB} = 0, \\
K_{SS} &= [TR]^T[K_{SS}]'[TR]
\end{aligned}$$

where $K'_{SS} = \int {D_u}^T D(\xi) D_u dz$ and

$$[TR] = \begin{bmatrix} \cos\theta & \sin\theta & 0 & 0 \\ -\sin\theta & \cos\theta & 0 & 0 \\ 0 & 0 & \cos\theta & \sin\theta \\ 0 & 0 & -\sin\theta & \cos\theta \end{bmatrix},$$

θ is the angle at which SMA wire is placed with in the aerofoil. The elements of force vectors are obtained as

$$\begin{aligned} F_A &= \int {N_w}^T P^+ \lambda dx, \\ F_B &= \int {N_w}^T P^- \lambda dx, \\ F_S &= [TR]' F'_S, \end{aligned}$$

where

$F'_S = \int {D_u}^T [\sigma_0 - D(\xi_0)\epsilon_0 - \epsilon_l D(\xi)\xi_s + \epsilon_l D(\xi_0)\xi_{s0} + \theta(T - T_0)] dz.$

F_A and F_B denote the forces acting on the aerofoil due to aerodynamic pressure distribution and F_S denotes the force exerted by the SMA wire. This force F_S varies with the temperature of the SMA wire which in turn changes F_A and F_B as the aerofoil coordinates are updated at each temperature step. The stiffness coefficient of SMA (D) is a function of temperature and so the stiffness of the SMA wire varies with each temperature step. σ_0 is the prestress given to the SMA wire and the value should be closer to the transformation plateau or the transformation criteria (${\sigma_s}^{cr}$).

Finite element siffness matrices and the nodal force vectors are formed based on the above equations and then they are assembled. A MATLAB code has been developed for this purpose. Finally the deflections of the aerofoil at each node are obtained. Detailed procedure for computing the aerodynamic pressure and the coupled iterative solution framework are discussed next.

3.3 Potential flow computation by panel method

Panel method was developed by Hess and Smith [48] at Douglas Aircraft Company. Panel methods are ideal for concept design analysis due to their rapid turnaround time and relatively easy surface modeling, but this is countered by their inability to predict boundary layers and flow separation. The lack of viscosity modeling in a panel method leads to another limitation: they cant model rotational flows such as that found in a cyclone. Panel methods cant model supersonic flow (Mach number ¿ 1) either.

The equations governing 2-D, incompressible, irrotational flow are:

- Continuity:

$$\frac{\partial u}{\partial x} + \frac{\partial v}{\partial y} = 0 \tag{3.17}$$

- and Irrotationality

$$\frac{\partial u}{\partial y} - \frac{\partial v}{\partial x} = 0 \tag{3.18}$$

The velocity potential Φ can be defined as

$$\frac{\partial \Phi}{\partial x} = u, \quad \frac{\partial \Phi}{\partial y} = v. \tag{3.19}$$

Then the continuity equation (Eq: 3.17)becomes a Laplace equation.

$$\frac{\partial^2 \Phi}{\partial x^2} + \frac{\partial^2 \Phi}{\partial y^2} = 0 \tag{3.20}$$

The governing equation (Laplaces equation) is recast into an integral equation. This integral equation involves quantities such as velocity, only on the surface, whereas the original equation involved the velocity potential Φ all over the flow field.

In this method, when an aerofoil is placed in a uniform flow of speed U, the velocity potential due to the uniform flow is superimposed on the velocity potential due to the

disturbed flow around a body to obtain the total velocity potential (Φ); that is,

$$\Phi = Ux + \phi \tag{3.21}$$

where Ux is the free-stream potential and ϕ is the disturbance potential. This disturbance potential around the aerofoil can be modelled by a distribution of sources and vortices over the surface. In our computational scheme, the Kutta condition is satisfied with the help of the condition that the magnitudes of velocities on the upper and the lower surface approach the same limiting value as the trailing edge is approached. The aerofoil surface is discretized into N number of panels. Sources and vortices of uniform strength per unit length are assumed to be acting over each panel. The sources and vortices distributed over a panel j induce a velocity $\vec{V}_{ij}$ at the collocation point of panel i. The normal velocity V_{ni} and the tangential velocity V_{ti} at the collocation point i are given by

$$V_{ni} = \sum_{j=1}^{N} \bar{p}_j N_{ij} + \gamma N_{i,N+1} + \vec{U} \cdot \hat{n}_i \ , \tag{3.22}$$

$$V_{ti} = \sum_{j=1}^{N} \bar{p}_j \bar{t}_{ij} + \gamma \bar{t}_{i,N+1} + \vec{U} \cdot \hat{t}_i \ , \tag{3.23}$$

where $\hat{n_i}$ and $\hat{t_i}$ are the unit normal and the tangential vectors, respectively. N_{ij} and $\bar{t}_{ij}$ are the normal and tangential influence coefficients, respectively. $\bar{p}$ denotes the source strength per unit contour and γ denotes the vortex strength per unit length. Since the surface represented by the panel is a solid surface, perpendicular velocity at each collocation point must be zero or prescribed by the aerofoil surface velocities obtained from the previous solution step. This condition gives N equations, which are supplemented by the Kutta condition giving a total of $N + 1$ equations. The Kutta condition states that "As the trailing edge is approached, the magnitudes of the velocities on the upper and lower surfaces approach the same limiting value" as illustrated in Fig. 3.3. The Kutta condition can be written mathematically by equating the magnitudes of the tangential

velocities at the collocation points of the two panels defining the trailing edge as follows.

$$\sum_{j=1}^{N} \bar{p}_j \bar{t}_{r,j} + \gamma \bar{t}_{r,N+1} + \vec{U} \cdot \hat{t}_r = -(\sum_{j=1}^{N} \bar{p}_j \bar{t}_{r+1,j} + \gamma \bar{t}_{r+1,N+1} + \vec{U} \cdot \hat{t}_{r+1}) \ . \tag{3.24}$$

Here the subscripts r and $r+1$ denote the panels connecting the trailing edge. By solving

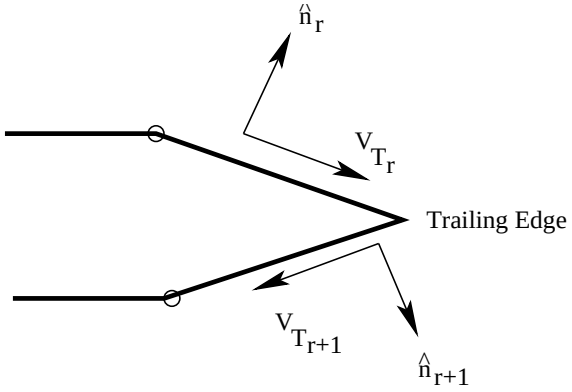

Figure 3.3: Method of implementing Kutta condition at the trailing edge

Eqs. (3.22) and (3.24), we get N number of source strengths per unit length and vortex strengths per unit length. The tangential velocities are obtained from Eq. (3.23) at each panel. The pressure at each collocation point i is calculated with the help of the Bernoulli equation. The coefficient of pressure at the collocation points is obtained as

$$C_{p_i} = 1 - (\frac{V_{ti}}{U})^2 \ . \tag{3.25}$$

Distribution of coefficient of pressure is then obtained over the chord length and it is used in the determination of coefficient of lift.

3.4 Results and discussions

3.4.1 A Coupled Fluid-Structure Interaction Model without SMA Wire

The deformations of the upper and lower skins of the aerofoil are obtained by solving fluid−structure interaction problem in COMSOL MULTIPHISICS. Transient analysis of incompressible Navier−Stokes model is carried out to obtain the pressure distribution over the aerofoil and the deformation of the aerofoil due to the aerodynamic pressure is obtained by considering the plane strain condition. Two domains, one for the fluid and other for the strucure (aerofoil) are created. Incompressible Navier−Stokes equation is solved in the fluid domain and it is coupled with the structural domain to obtain the aeroelastic deformations of the aerofoil.

Fig. 3.4 shows the mesh grid of the fluid−structure domain. A triangular mesh is used with an element aspect ratio of 0.0023 and the number of degrees of freedom solved are 68795. The solution is obtained by using the Direct(UMFPACK) solver. The boundary conditions used are similar to the conditions discussed in the Sec. 3.2.

Fig. 3.5 shows the multiphysics analysis carried out for a free stream velocity of 20

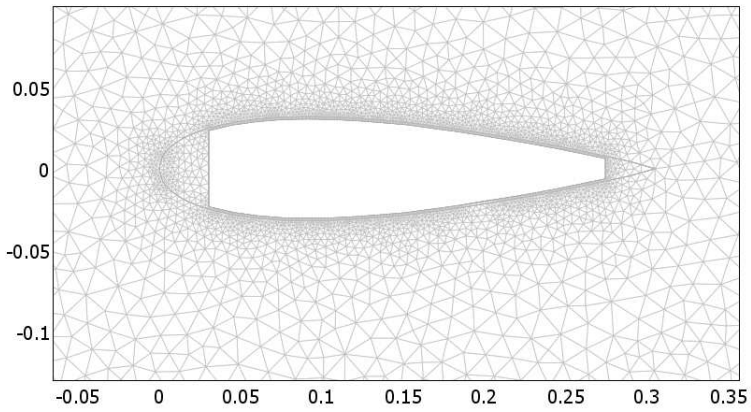

Figure 3.4: Mesh grid of the fluid-structure domain

m/s. The model is solved for 0.1 seconds with a time step of 0.005 sec. The aeroelastic deformation of the aerofoil is shown in the Fig. 3.6. There is a maximum deflection of 0.1 mm and these deflections at the maximum thickness location and the trailing edge are plotted against various free stream velocities as shown in Fig. 3.7. From this load-deflection curve we estimate the thickness of the skin to be used and the bias stress that need to be applied to the SMA wire for various operating speeds.

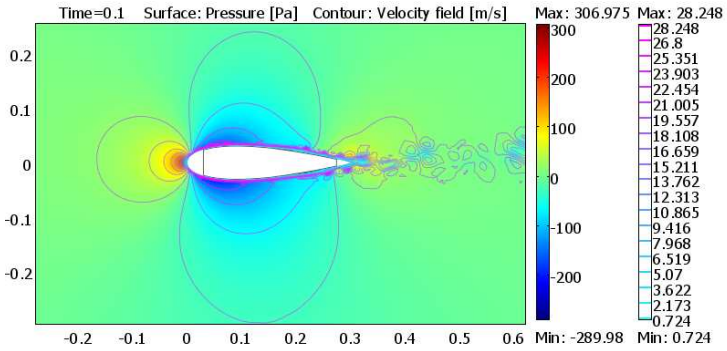

Figure 3.5: Velocity and Pressure countours over the aerofoil

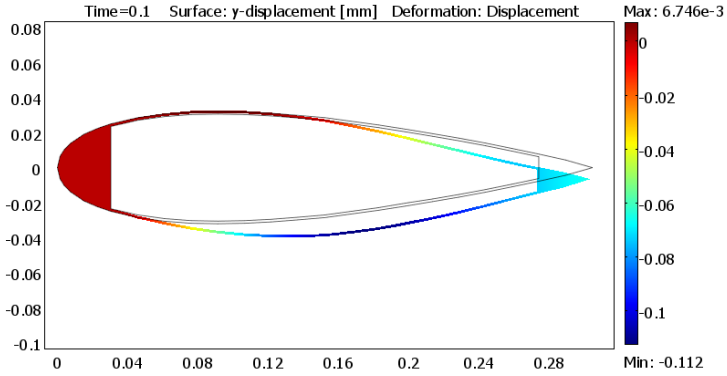

Figure 3.6: Aeroelastic deformation of the aerofoil

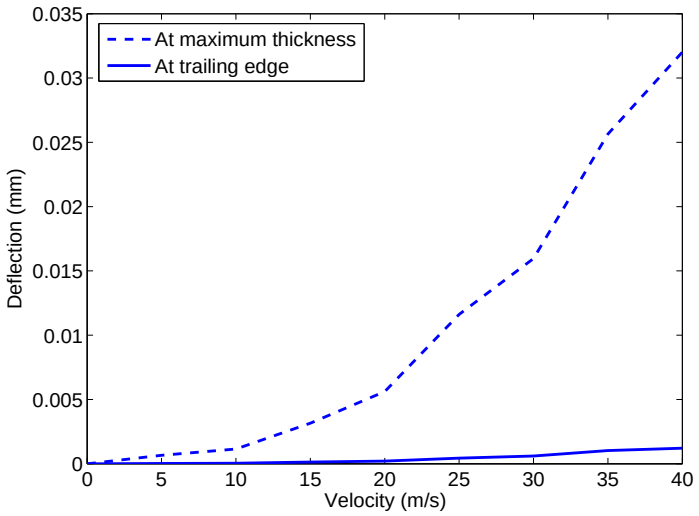

Figure 3.7: Deflections of aerofoil at maximum thickness location and at the trailing edge for various operating speeds

From the above results, the thickness of the aerofoil is chosen as 1mm and is used in the further analysis to obtain the hysteritic deflections of the aerofoil corresponding to the hysteritic deformation of SMA wire with the developed computational model.

3.4.2 A Coupled FE Model of Aerofoil with Aerodynamics based on Potential Flow

A preliminary analysis of fluid-structure interaction problem is solved in COMSOL to estimate the aeroelastic deformations of the aerofoil. When the SMA wire is actuated, its properties keep changing with increment in the temperature and so coupling of SMA wire model with the fluid-structure interaction will be a difficult task. So, a computational model is developed as described in Sec. **??**The deflection of the aerofoil is calculated based on the finite element model developed in Sec. 3.2 to capture the hysteritic deformation of SMA wire. By using the developed computational model, the deflection of the aerofoil can be captured over the entire hysteris range and the variation in the c_l with the actuation can be obtained. The fluid-structure coupling is done in a self-consistent

manner. The panel method discussed in Sec. 3.3 is employed to obtain the coefficient of pressure variation over the deformed aerofoil. A free stream velocity of 20 m/s, free stream pressure of 1 bar and air density 1.225 kg/m^3 and 1 mm thick aluminium skin are considered in the simulation. As described earlier, the SMA wire is attached to the upper and the lower surfaces of the aerofoil and it is used in deflecting the aerofoil following a hysterisis loop. The SMA wire can be actuated either by applying stress (a bias stress plus a dynamic actuation) or temperature (electrical heating) or both. By controlling the stress or temperature in the SMA wire, it is possible to alter the lift produced by the aerofoil. A scheme for the developed coupled analysis framework is shown in Fig. 3.8. This coupled scheme is followed to obtain the hysteritic deflections of the aerofoil.

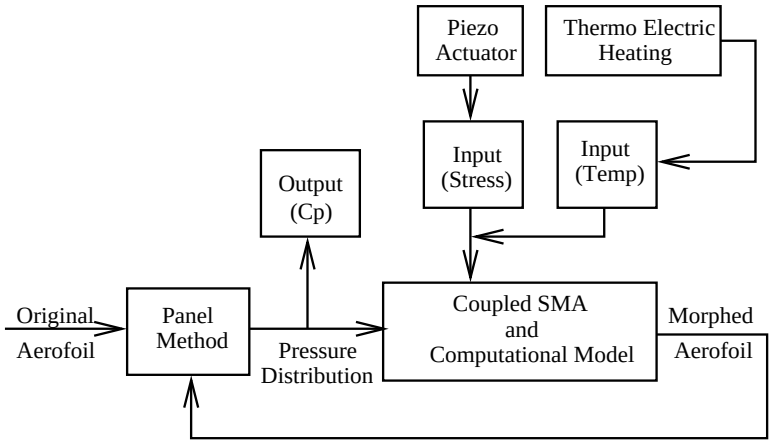

Figure 3.8: Coupled analysis scheme

As shown in the block diagram (ref 3.8), the co−ordinates of the original aerofoil are used to obtain the pressure distribution using the panel method. This aerodynamic pressure along with the force exerted by SMA wire (either by stress or temperature) are sent into the coupled computational model. The co−ordinates the deformed/morphed aerofoil are used again to calculate the variation in c_p and c_l. This data is stored and the updated co−ordinates are used again for the next pseudo−time step. In this way the iteration goes on and the deformation of the aerofoil along with the change in c_l are obtained over the entire hysterisis of SMA behaviour.

The procedure for obtaining the SMA wire actuation force (F_s) over the entire hysterisis

is shown as a flowchart in Fig. 3.9 and is followed in the present simulations. For the temperature induced transformation of SMA wire, the incremental stress obtained from the constitutive model is applied on the aerofoil and the corresponding deflection of the aerofoil is employed to compute the differential strain of the SMA wire due to aerofoil stiffness. This differntial strain is used back in the constitutive model along with the ξ, D and σ updates to obtain the incremental stress for the next temperature step. The procedure is simple in the case of stress induced transformation of SMA wire as the incremental stress given to the wire is directly applied on the aerofoil and the corresponding deflection of the aerofoil is calculated.

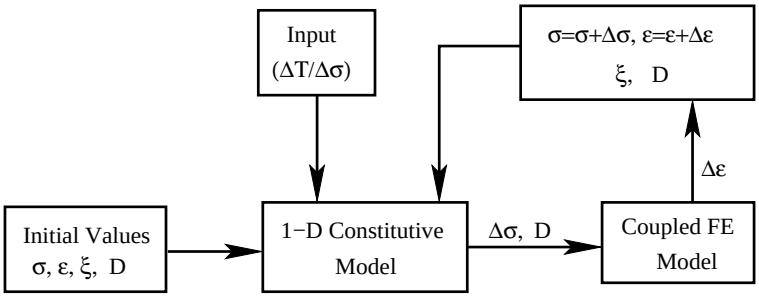

Figure 3.9: Computational scheme for obtaining the force in the SMA wire actuator

3.4.3 SMA Wire Properties

The material properties of the shape memory alloy in the present numerical simulations are taken from ref. [46] and are listed in Table 3.1.

Material Constants	Transformation Temperatures	Transformation Constants	Maximum Residual Strain
$D_a = 67$ Gpa $D_m = 26.3$ Gpa $\Theta = 0.55$ Mpa/^0C	$M_f = 9^0C$ $M_s = 18.4^0C$ $A_s = 34.5^0C$ $A_f = 49^0C$	$C_M = 8$ Mpa/^0C $C_A = 13.8$ Mpa/^0C $\sigma_s^{cr} = 100$ Mpa $\sigma_f^{cr} = 170$ Mpa	$\epsilon_l = 0.067$

Table 3.1: Material properties of SMA wire.

For the stress induced transformation of SMA wire, the wire has to be maintained at room temperature Austenite. This is necessary to achive pseudoelastic effect as the stress has to be applied when the SMA wire is maintained above Austenite start (A_s) temperature. As the SMA wire is elongated with the rise in stress, it can not apply any force on the aerofoil and so the aerofoil has to pre-stressed before the actuation.The aerofoil gets relaxed with the elaongation of SMA wire and the morphing is achieved in this way. During unloading the stress, the SMA wire contracts and pulls the aerofoil skin to the original configuration.

For the temperature induced transformation of SMA wire, the wire has to be maintained at room temperature Martensite as the wire gets contracted with the rise in temperature. The material transforms to Austenite phase as the temperature reaches Austenite finish (A_f). Pre-stress in the aerofoil is not required as the SMA wire is going to apply force on the aerofoil during temperature rise and relaxes during unloading. So, SMA wire has to be maintained at two different states depending on the type of triggering of phase transformation.

3.4.4 Morphing due to stress-induced transformation of SMA wire

As discussed earlier, the SMA wire can be actuated either by stress or temperature induced transformation, this section deals with the former case. SMA wire can be placed at various possible locations in the aerofoil and one of such possible locations for placing the SMA wire joint that we analyze here is the location of the maximum thickness of the aerofoil. The simulation is carried out with the free stream velocity of 20 m/s at 5^0 angle of attack. Prestress is applied to the aerofoil to accommodate the expansion of the SMA wire when stress is applied to it. Stress is varied incrementally over the hysterisis range and the deflection of the aerofoil is captured at each stress increment using the coupled finite element model and corresponding variation in the coefficient of pressure (c_p) is obtained from the panel code. Calculations are done for vertical and inclined positions of SMA

wire at two different temperatures 50^0C and 60^0C. Further investigation is carried out to identify the optimum position of SMA wire which gives maximum coefficient of lift (c_l) over the chord length. This is done by placing the wire at three different locations. The inclined position of the SMA wire is optimized based on the amount of trailing edge deflection obtained. The main objective of vertical positioning of the SMA wire is to vary the aerofoil thickness, where as the objective of angular positioning is to achieve a trailing edge deflection of the aerofoil. The panel method described in the Sec. 3.3 is used to obtain the coefficient of pressure variation over the aerofoil. Figs. **??** shows the deformed shapes of the aerofoil when the SMA wire is positioned vertically within the aerofoil and the variation in the aerofoil thickness for three different locations of SMA wire over the chord length is shown in Table. 3.2. It is observed that the thickness variation is large when the SMA wire is placed at 25% of the chord than at the other two locations. It is also observed that the variation is a bit higher when the SMA wire is maintained at 60^0C than at 50^0C. This is mainly due to the higher stress values required for the transformation to take place when the SMA wire is maintained at 60^0C. The c_p distribution is shown in Fig. 3.12.

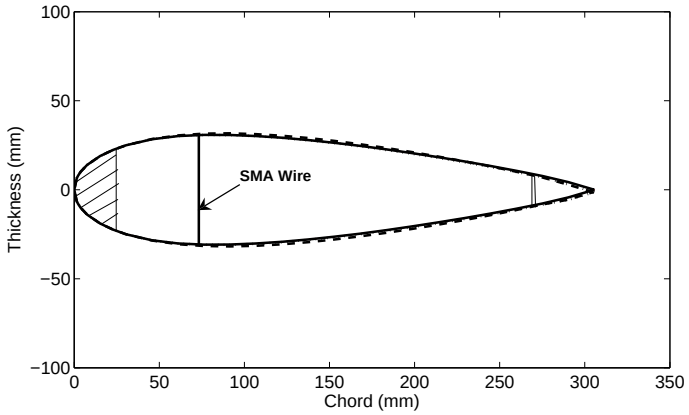

Figure 3.10: Deflection of the aerofoil when SMA is placed at 25% of chord at 50^0C

Figures. 3.13 and 3.14 shows the deformed shapes of the aerofoil for the angular position of SMA wire placed within the aerofoil for two different temperatures 50^0C and 60^0C, respectively. The deformed shapes of the aerofoil for selected points on the hysterisis curve are plotted to show the deflection pattern of the aerofoil over the entire hysterisis.

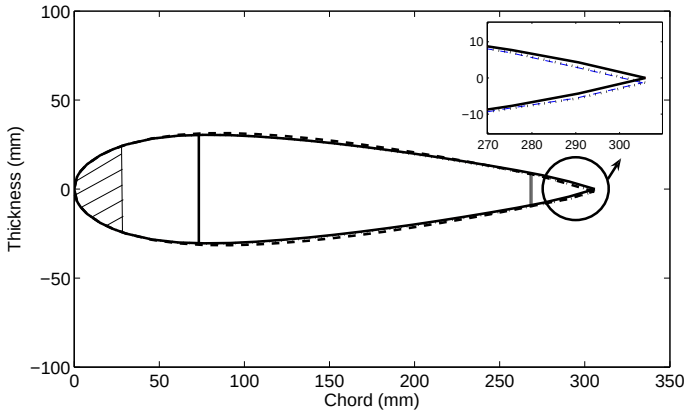

Figure 3.11: Deflection of the aerofoil when SMA is placed at 25% of chord at 60^0C

Temperature	Chordwise location of SMA wire		
	25%	30%	50%
50^0C	2.81%	1.72%	0.63%
60^0C	3.44%	1.87%	0.78%

Table 3.2: Maximum thickness variation (% of maximum thickness) when the SMA wire is placed at three different locations over the chord length.

The zoomed trailing edge deformations are shown in the Figs. 3.13(c) and 3.14(c). The numbering $(1-7$ and $1-8)$ given on the hysterisis curve indicates the loading and unloading pattern with the pre−stress given to the wire. The c_p distribution is shown in Fig 3.15. It is observed that the trailing edge is deflected by 5.1 mm and 5.7 mm for the 50^0C and 60^0C cases, respectively.

The coefficient of lift (c_l) keeps changing with every pseudo-time step and it is plotted against the corresponding stress value in the SMA wire for 60^0C as shown in Fig 3.16. The variation in c_l is about 12% and 15% for 50^0C and 60^0C, respectively.

3.4.5 Morphing due to temeprature-induced transformation of SMA wire

The SMA wires are electrically heated up to induce the phase transformation from martensite to austenite. The temperature is raised slowly in a quasi-steady manner by increasing

the current applied to the SMA wires. The strain caused in the SMA wire due to the rise in temperature is actually constrained by the stiffness of the aerofoil and this increases the stress in the SMA wires. The increase in stress of the SMA wires at each temperature step along with the aerodynamic load is applied to the aerofoil in a finite element sense and the deformed aerofoil shape is obtained at each step.

The SMA wire is given a prestress (σ_0) of 50 MPa considering it to be in martensite phase. Thae values of ξ_{s0}, ξ_{T0} and ϵ_0 are taken as 1, 0 and 5 respectively. There is a trailing edge deflection of 4.6 mm when two SMA wires are used. This deflection would have been larger for a less stiffer aerofoil. But a less stiffer aerofoil will not sustain the aerodynamic loading and the SMA wire will get strained without any actuation and the entire purpose of morphing will not be achieved. Fig. 3.17(a) shows a variation in the stress in the SMA wire for a single thermal loading cycle. Fig. 3.17(b) shows the original and the deformed shapes of the aerofoil for the inclined position of SMA wire. The trailing edge deflection and the variation of coefficient of lift (c_l) with respect to temperature are shown in Fig. 3.18. The c_p distribution is shown in Fig 3.19. As seen from the Fig. 3.18, the trailing edge deflection and the coefficient of lift followed the trend of stress variation in the SMA wire.

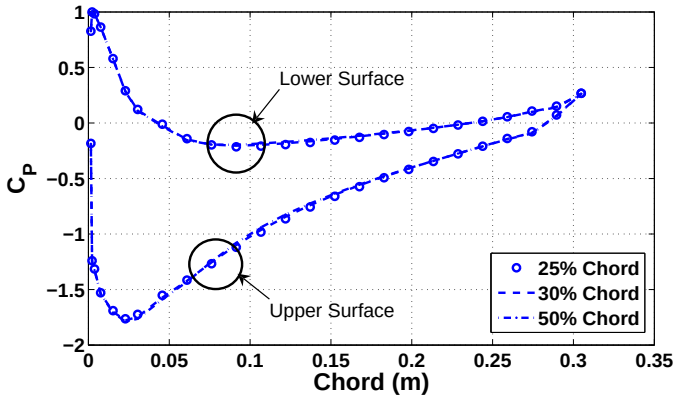

(a)

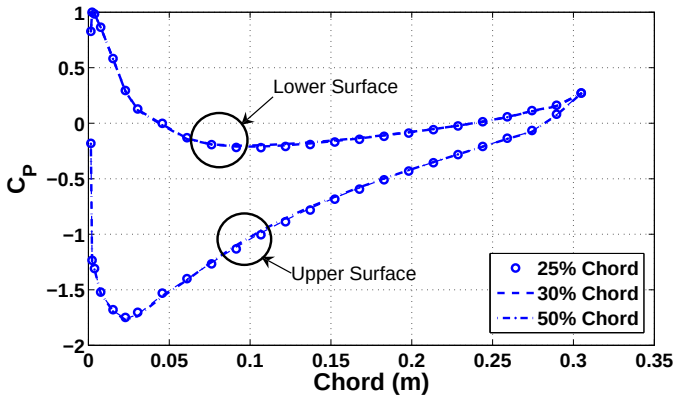

(b)

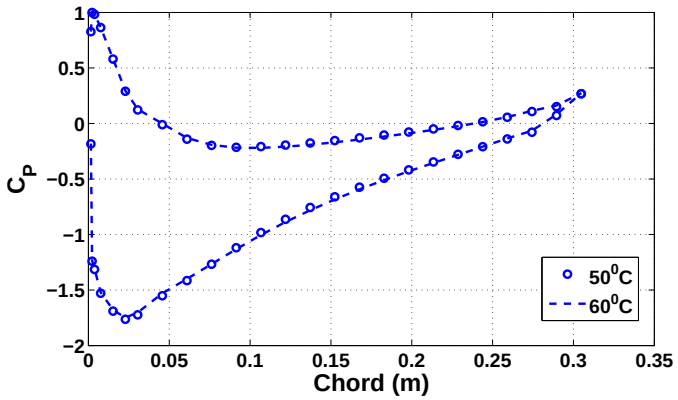

(c)

Figure 3.12: Variation in the coefficient of pressure (c_p) over the aerofoil when the SMA wire is placed at three different locations of the chord at (a) 50^0C(b) 60^0C, (c) Variation of coefficient of pressure over the aerofoil when SMA wire is placed at 25% of chord for two different temperatures.

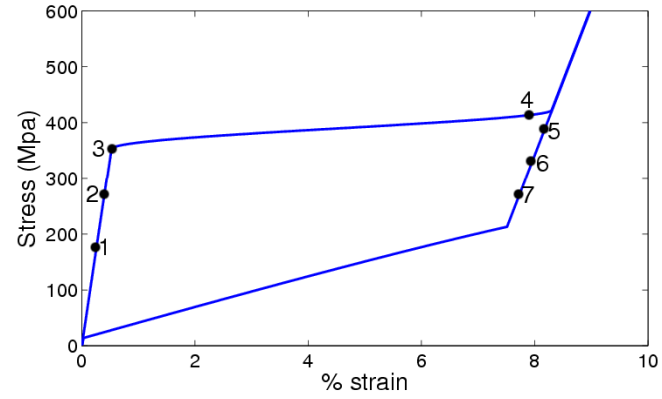

(a)

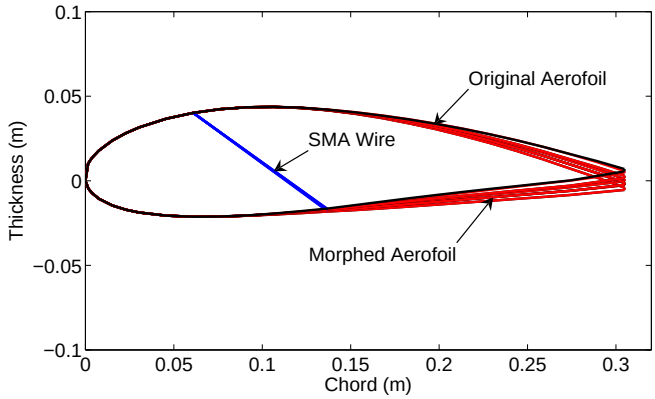

(b)

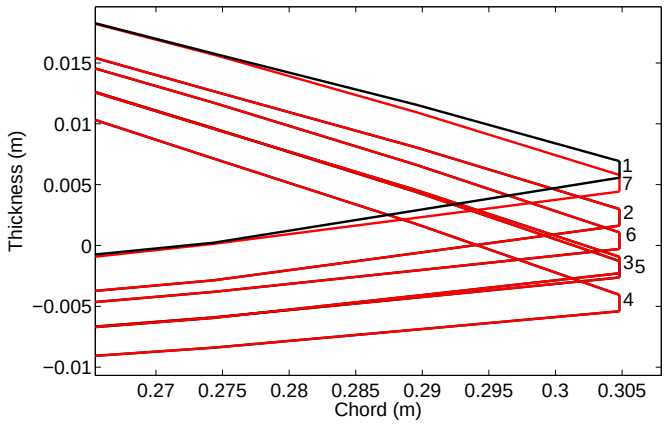

(c)

Figure 3.13: (a) Stress-strain hysterisis curve for the SMA wire for stress induced transformation at 50^0C. State of the deformed aerofoil at various stages of actuation are tracked at the points marked on the hysterisis curve. (b) Original and Morphed configurations of the aerofoil for one cycle of actuation of SMA wire at 50^0C. (c) Trailing edge deflection corresponding to the actuation (see (a)) at 50^0C.

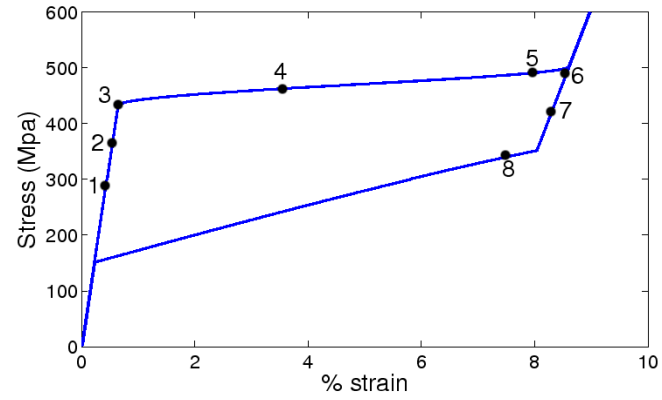

(a)

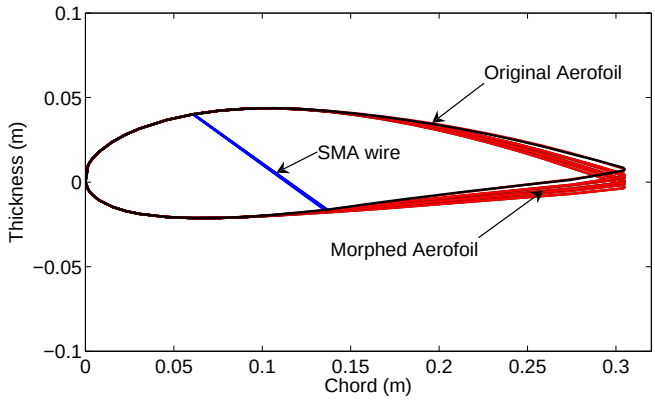

(b)

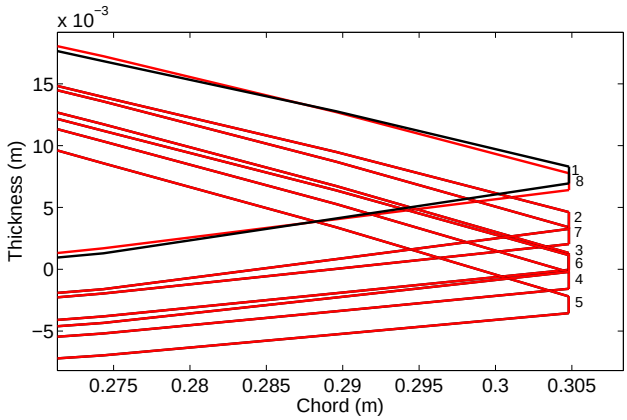

(c)

Figure 3.14: (a) Stress-strain hysterisis curve for the SMA wire for stress induced transformation at 60^0C. State of the deformed aerofoil at various stages of actuation are tracked at the points marked on the hysterisis curve. (b) Original and Morphed configurations of the aerofoil for one cycle of actuation of SMA wire at 60^0C. (c) Trailing edge deflection corresponding to the actuation (see (a)) at 60^0C.

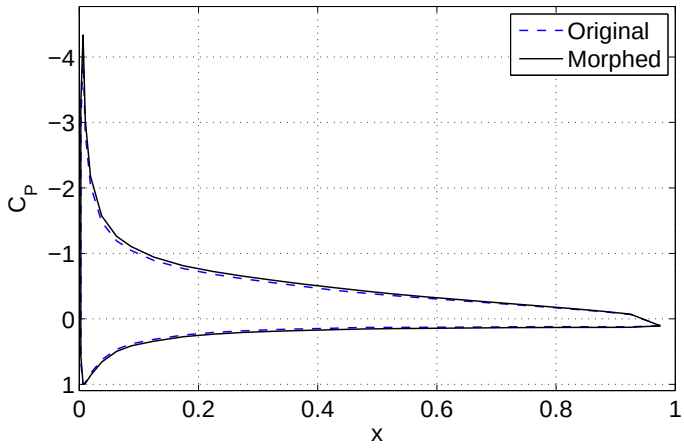

(a)

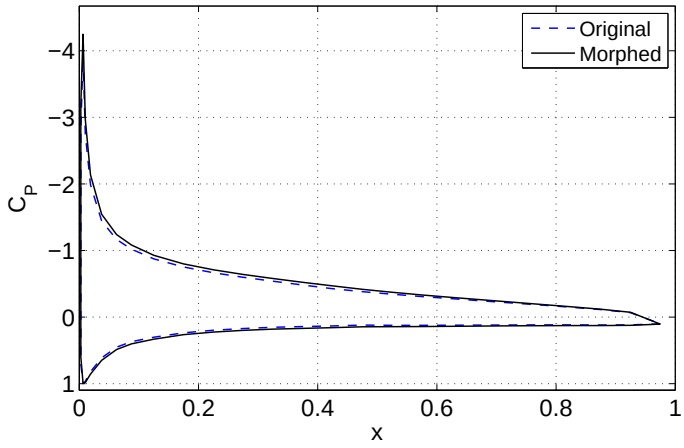

(b)

Figure 3.15: (a) Variation in the coefficient of pressure (c_p) over the aerofoil for the angular placement of SMA wire at 50^0C (b) Variation in the coefficient of pressure (c_p) over the aerofoil for the angular placement of SMA wire at 60^0C.

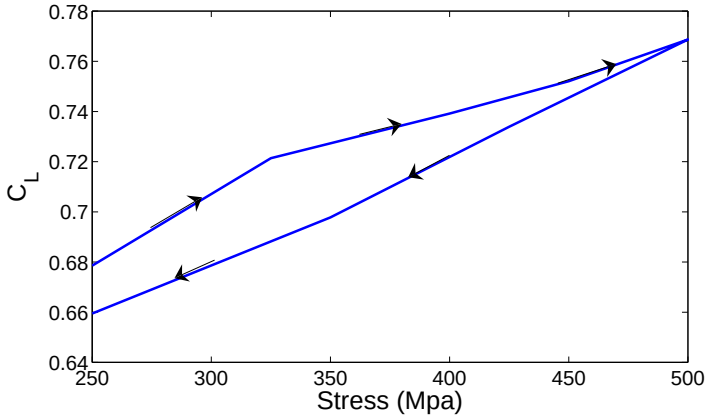

Figure 3.16: Variation in the coefficient of lift (c_l) as a function of stress induced transformation of SMA wire.

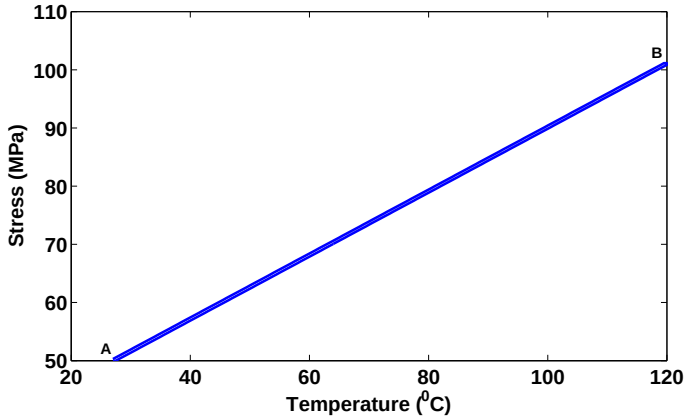

(a)

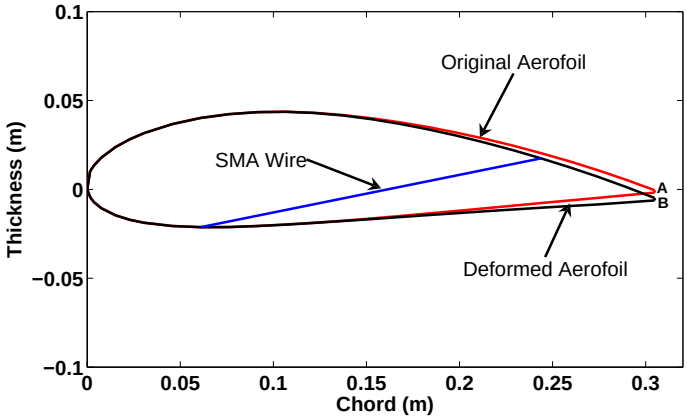

(b)

Figure 3.17: (a) Variation in the stress in the SMA wire for a single thermal loading cycle (b) Original and deformed shapes of the aerofoil.

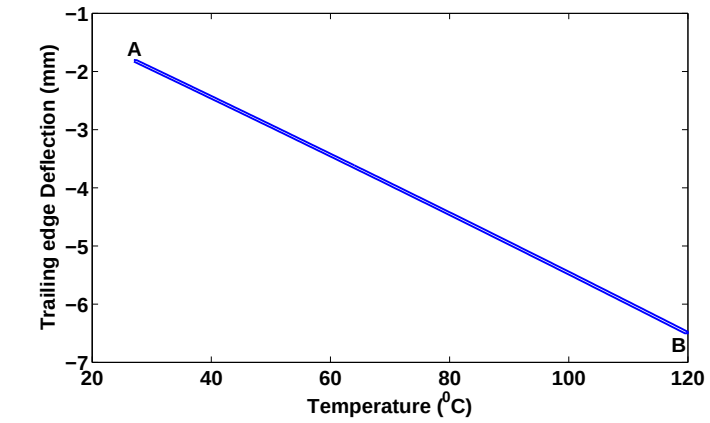

(a)

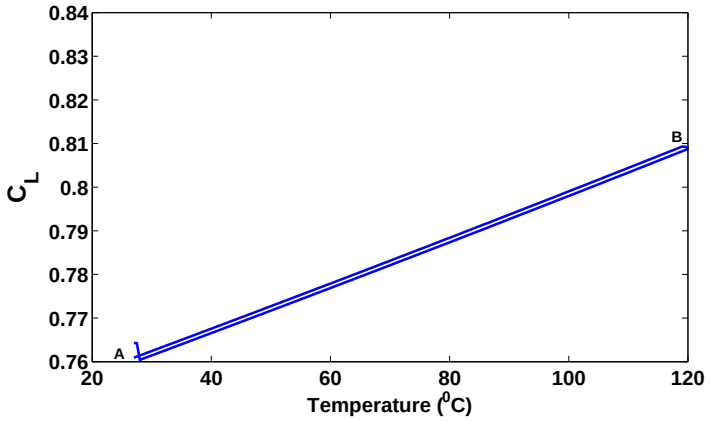

(b)

Figure 3.18: (a) Variation in the trailing edge deflection for one thermal loading cycle (b) Variation in the coefficient of lift (c_l) for a single thermal loading cycle.

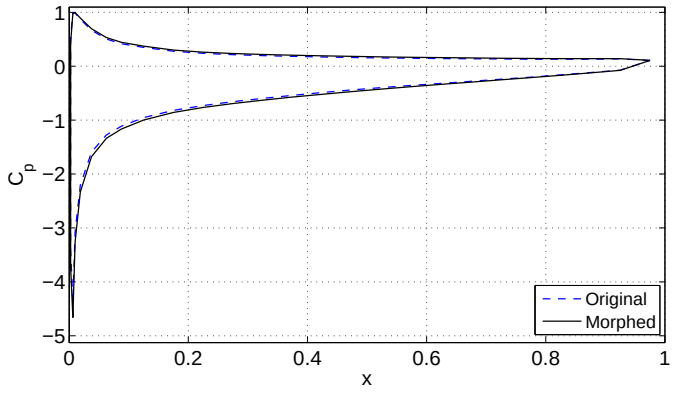

Figure 3.19: Variation in the coefficient of pressure (c_p) over the aerofoil for a single thermal loading cycle.

Chapter 4

Experimental Study

The main objective of this experimental study is to realize a morphing wing in accordance with the simulations carried out. The simulations carried out in Chap. 3 will be used here to optimize the performance of the morphing system. The preliminary analysis done from the simulations for various configurations of SMA wire is put into practice to design a morphing wing. As described earlier, the transformation of SMA wire can be achieved by either varying stress or temperature. It is easier to achieve temperature induced transformation than stress induced transformation because the latter case needs pre-stressing of the aerofoil. Various aerofoil models are designed, fabricated and tested using thermo-electrical heating. The SMA wires are transformed by thermo-electrical loading and the corresponding trailing edge deflection of the aerofoil is measured using laser sensor (Keyance-LK-G82). The temperature of the SMA wire is measured using a thermocouple and is read in the computer through Data Aquisition System (DAQ) system. The experimental procedure is shown as the schematic diagram in Fig. 4.1. A LabVIEW circuit has been designed to send input and output signals from and to between the SMA wire and the computer. A brief discussion of the circuit is given in the next section.

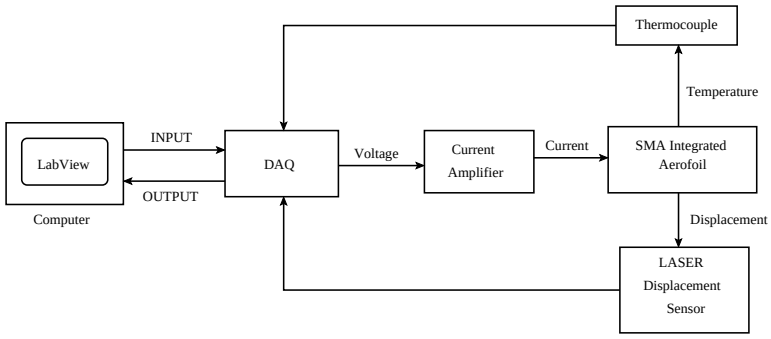

Figure 4.1: Experimental analysis scheme

4.1 LabVIEW Circuit Design

LabVIEW (short for Laboratory Virtual Instrumentation Engineering Workbench) is a platform and development environment for a visual programming language from National Instruments. A LabVIEW circuit has been developed for sending the required amount of current in a systematic manner to the SMA wires. It is also used for receiving the trailing edge displacement from the Laser sensor and the temperature from the thermocouple. The designed LabVIEW circuit is shown in the Fig. 4.2. A MATLAB script file is used to

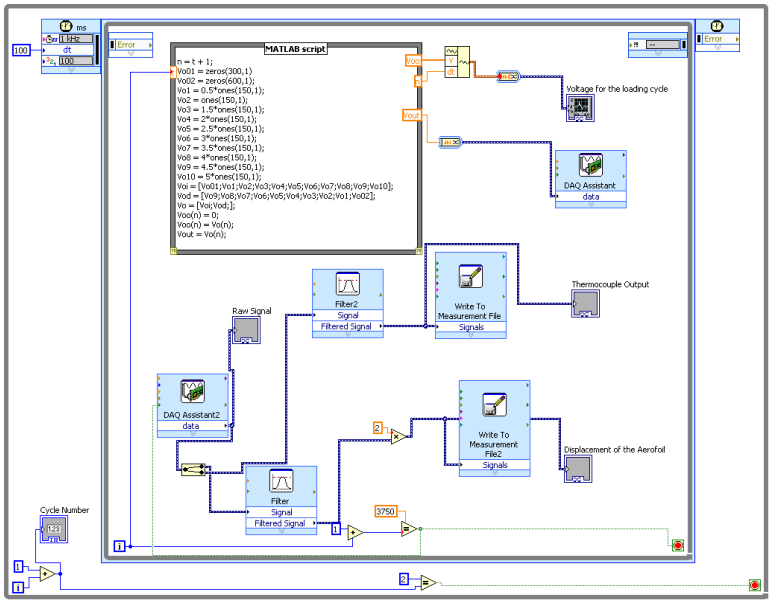

Figure 4.2: LabVIEW Circuit

send the voltage input in steps to the current amplifier through DAQ. The output from

the Laser sensor is in voltage which is converted to displacement using the LabVIEW. The input voltage to the current amplifier, the displacement of the aerofoil and the temperature of the SMA wire can be monitored and can be stored in a file. The post processing of the data is done in MATLAB and finally displacement of the aerofoil is plotted against the temperature of the SMA wire. The SMA wires are heated up using thermo-electrical actuation and the principle of electrical current based heating is discussed in the next section.

4.2 Principle of thermo-electrical actuation of SMA wire

The ability of the SMA wires to contract is dependent upon Joule heating to produce the transformation temperature required. Similarly, the ability of the SMA wires to return to their original configuration is dependant upon the ability of the system to cool the wires. The heat source for the wires is provided by Joule heating, the application of current. The heat transfer in the wires is also affected by latent heat due to the phase transformation of the material. The heat sink for the wires is provided by natural convection to the air surrounding the wires. The heat transferred to the surrounding air inside the wing by the wires thus acts as the structural heat source, wherein heat is conducted to the aluminum structure. The entire system is then cooled by convection to the surrounding air, providing the structural heat sink.

A thermodynamic model can be applied to the heating and cooling of the wires. This model is based on the lumped system analysis, assuming that the conduction of heat at the ends of the wires is negligible in comparison to the convection of heat to the environment. This assumption is supported by the fact that the cross sectional area of the wire is very small in comparison to the surface area of the long wire. Conservation of energy thus defined the equation used to predict the heating and cooling of the wires in time. The heat transfer model defined in Eq. 4.1 is based on material properties of the SMA wires,

the heating source, and natural convection.

$$-mc_v\dot{T} + W - hA(T - T_\infty) = 0 \tag{4.1}$$

where T is the surface temperature, T_∞ is the ambient temperature and Wrepresents the heating source, defined by Joule heating as follows

$$W = i^2R \tag{4.2}$$

where i is the current passed through the wire and theThe heating solution of the model can thus be defined as follows,

$$T = T_\infty + \frac{W}{hA}[1 - exp(-D\tau)] \tag{4.3}$$

where the time constant, D, is defined by

$$D = \frac{hA}{mc_v} \tag{4.4}$$

Similarly, the cooling solution of the wire thermodynamic model is defined as follows:

$$T = T_\infty + (T_0 - T_\infty)exp(-D\tau) \tag{4.5}$$

The above equations describe the electrical current based heating of SMA wire. A Type K (Chromel / Alumel) thermocouple is used to measure the temperature of SMA wire. Various aerofoil configurations are tried out for maximizing the trailing edge deflection and the details of the fabricated aerofoil models are discussed in the next sections.

4.3 Small Aerofoil with Inclined SMA Wire

4.3.1 Rigid Aerofoil

A NACA4421 aerofoil is chosen for the experimental study as it has almost a flat bottommed skin which enhances bending of the upper skin when the SMA wires are connected from bottom skin to the upper skin. A wodden pattern is made with the available co−ordinates and the wing segment is fabriated using the pattern. The aerofoil is made of 1 mm thick aluminium sheet and the leading and trailing edge stiffeners are made of wodden blocks. The dimensional details of the aerofoil are shown as the schematic diagram in Fig. 4.3.

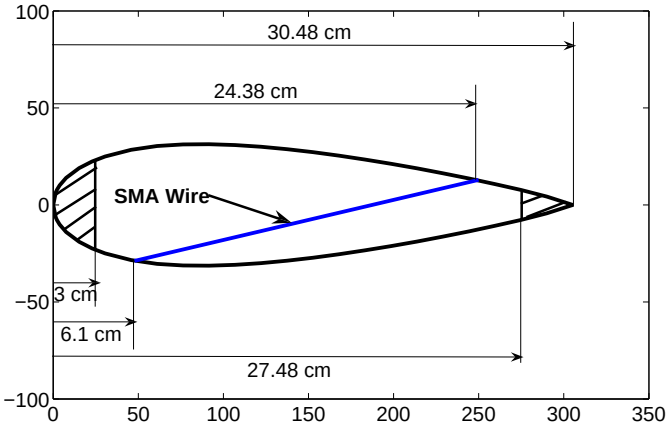

Figure 4.3: Schematic diagram of the aerofoil with integrated SMA wire

Current is passed through the wire incrementally from zero to 2 Amp using a current amplifier and DAQ. The temperature of the SMA wire is varied by controlling the current passed through it. The deformation of the SMA wire follows a hysterisis path for one complete thermal loading and unloading cycle. As the deformation of the SMA wire is constrained by the skins of the aerofoil, the stress in the SMA wire starts increasing which deforms the aerofoil. Assuming the force exerted by each SMA wire to be 6 N, two SMA wires are used in the aerofoil for the experimental study. As the aerofoil is a rigid one, there is a maximum trailing edge deflection of about 2.5 mm. This type of deflection is of no practical interest and a flexible aerofoil is fabricated which is discussed in the next

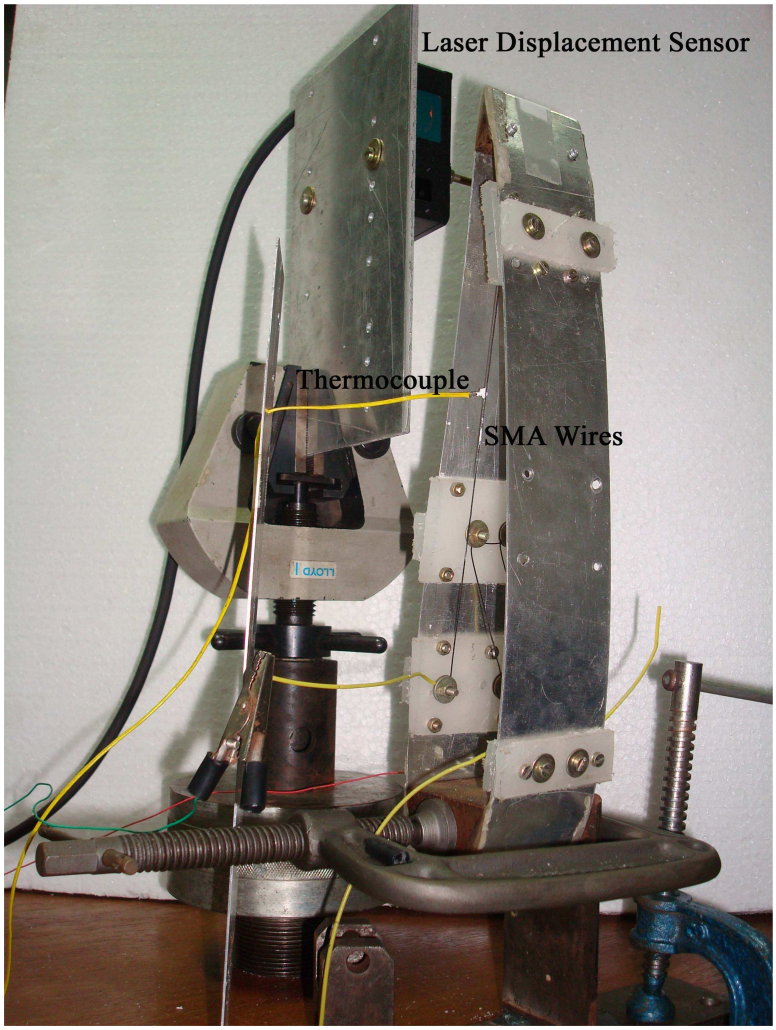

Figure 4.4: Fabricated aerofoil with integrated SMA wires

section.

4.3.2 Flexible Aerofoil with a Slider Mechanism

Various configurations of the aerofoil are analyzed to maximize the trailing edge deflection and one of such configuration is shown in Fig. 4.6. A portion of the rigid aerofoil is cut at a distance of 70% of the chord length and a flexible polyurethene sheet is placed at that position. The polyurethene sheet relaxes the bending stiffness of the aerofoil and allows for a greater trailing edge deflection. As the upper skin of the aerofoil is bent into convex shape using the SMA wires, the lower skin also has to bend in a similar fashion.

The stiffness of the lower skin does not allow the upper skin to bend too much and so a way is sorted out to over come this problem. A slider mechanism is placed on the lower skin which allow the lower aerofoil skin connected to the trailing edge moves towards the leading edge to accomodate the bending of the lower skin.

The linear slider mechanism used is shown in the Fig. 4.5. The part of the lower skin connected to the leading edge is fixed to the slider and the part connecting the trailing edge is allowed to move over the ball bearing. The bearing is attached to the aerofoil using the nut bolt arrangement. The bearing mechanism is placed at a distance of 60% of the chord length. The temperature variation in the wire and the trailing edge deflection

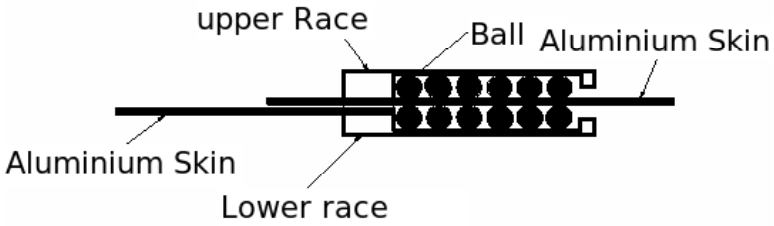

Figure 4.5: Ball bearing mechanism

is shown in Fig. 4.7. The variation of trailing edge deflection with temperature is shown in Fig. 4.8 follows a hystertic trend as exhibited by the SMA wire. There is a maximum trailing edge deflection of about 4 mm. As seen from the Fig.. 4.8, the temperature of the SMA wire reached 120^0C for a maximum current of 2 Amp.

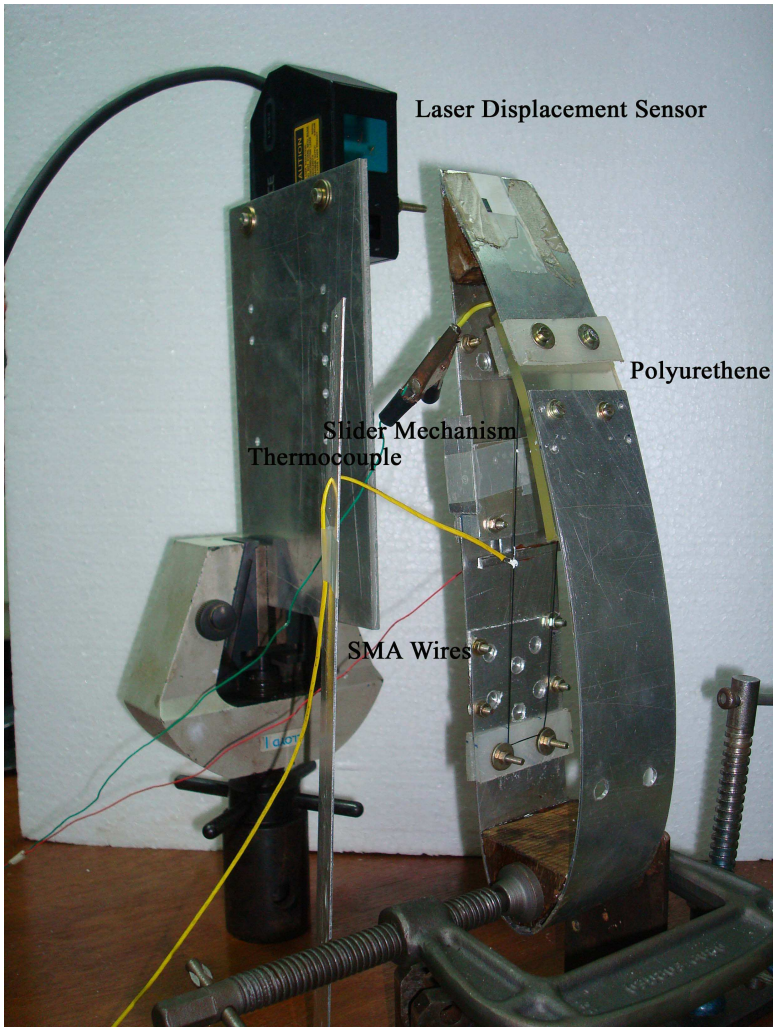

Figure 4.6: Experimental setup of the aerofoil integrated with SMA wires

The trailing edge deflection is not much for a flexible aerofoil even though a sliding mechanism is used. This is mainly due to the smaller gauge length of SMA wire available for actuation in such a smaller aerofoil. One way to increase the gauge length is to use a bigger aerofoil for the experimental study. The details of a bigger aerofoil model are discussed in the next section.

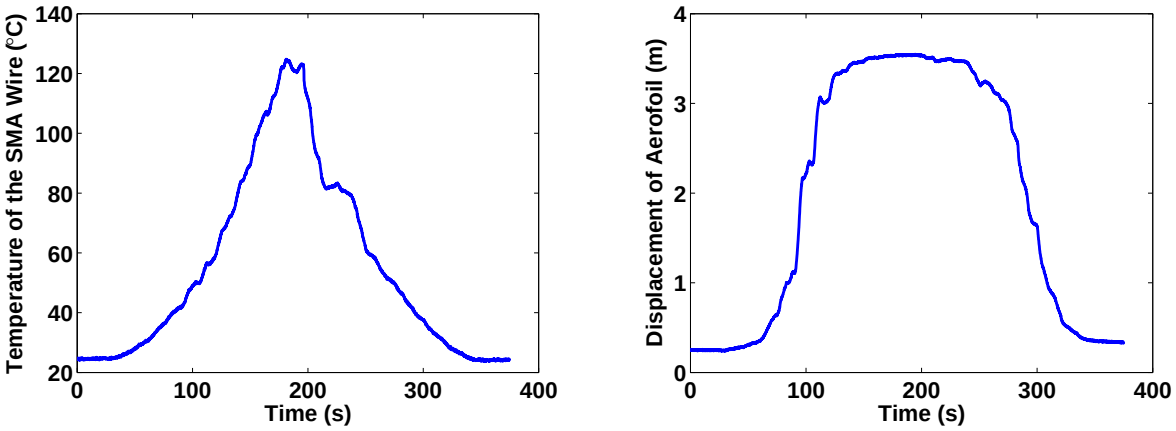

(a) (b)

Figure 4.7: (a) Temperature variation in the SMA wire (b) Trailing edge deflection of the aerofoil for a single thermal loading cycle

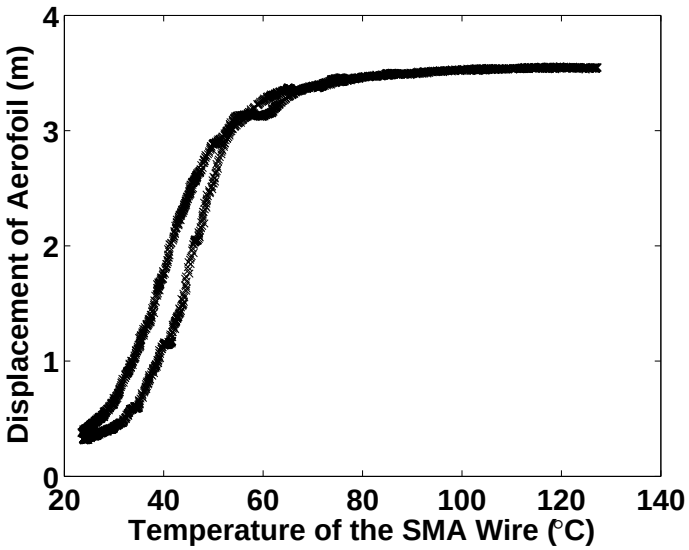

Figure 4.8: Variation of trailing edge deflection with temperature for one thermal loading cycle

4.4 Large aerofoil with SMA wire directly connected to a sliding mechanism

A large aerofoil of double the size of the smaller one (i.e., 2 feet chord length) is fabricated and is shown in the Fig. 4.9. In this aerofoil model, the SMA wires are not attached to the upper and lower skins of the aerofoil but they are attached to the slider itself on the lower skin. The part of the lower skin connected to the trailing edge is pulled towards the leading edge using the SMA wires and a greater trailing edge deflection is expected along with the thickness variation. Simulations are carried out in COMSOL to find out the number of wires and the location of the ball bearing for optimum trailing edge deflection keeping in mind the gauge length of SMA wire available. Fig. 4.10 shows the deformation of the aerofoil when a slider is placed on the lower skin of the aerofoil. Two SMA wires are used There is a trailing edge deflection of 17 mm when the slider is placed at a distance of 60% of the chord length for 260 mm gauge length of SMA wire.

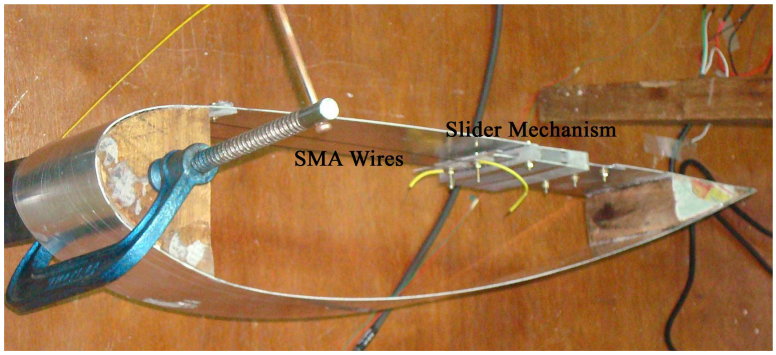

Figure 4.9: Experimental setup of the aerofoil with SMA wires connected to the slider mechanism

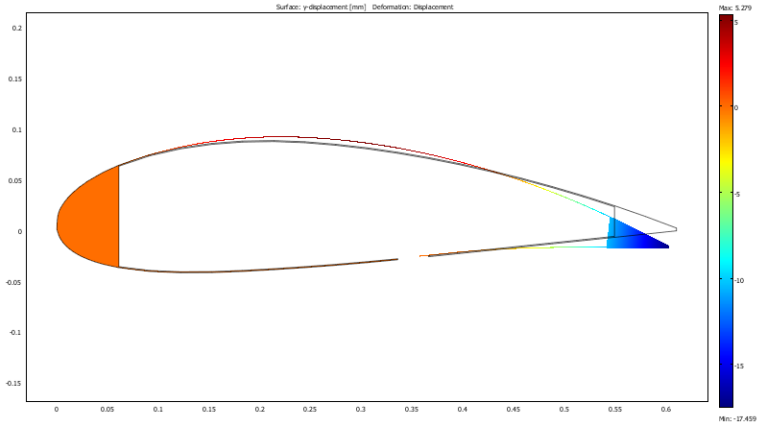

Figure 4.10: COMSOL simulation for a slider attachment on the lower skin

Chapter 5

Conclusions and Future Scopes

In the preliminary design of the morphing wing, the wing is divided into a the number of segments based on the aerodynamic pressure acting on the wing. The wing is divided into 18 segments and the analysis is carried out for one segment only.

Based on a coupled hysteretic model of SMA wire and a laminar incompressible flow over aerofoil, the deformed shapes of the aerofoil are obtained for various locations and positions of SMA wire. Various modeling issues in the coupled analysis are discussed. From the numerical simulations, we observed that the thickness variation is large when the SMA wire is placed at 25% of the chord than at the other two locations when positioned vertically. The variation in the coefficient of lift (c_l) is very less for the vertical position of SMA wire. The variation of c_l is about 12% and 15% for the angular placement of the SMA wire when actuated by stress-induced transformation at constant temperatures of 50^0C and 60^0C, respectively. We also observedthat the variation in the c_l is larger when the SMA wire is maintained at 60^0C than at 50^0C. Although the maximum strain is almost same in both the cases, however the difference in the variation of c_l is due to the higher stress required to change the SMA wire from austenite to martensite phase when the wire is maintained at 60^0C. For the temperature induced transformation of SMA wire, the variation of c_l is about 4% and this is due to the smaller stress values developed in the SMA wire. Instead of using a single wire, multiple wires may be used to obtain

larger deflections of the aerofoil. The trailing edge deflection can be maximized further by placing a less stiffer material at the point of application of load without compromising on aerofoil rigidity. An aerodynamically coupled finite element model for the SMA wire integrated aerofoil is developed and the simulations carried out are of great utility for the experiments carried out. The deformed states of the aerofoil and the corresponding variation in the c_l over the entire hysterisis are tracked and reported for both stress and temperature induced transformations of SMA wire.

Experiments are carried out for the various fabricated models. The fabricated aerofoils include a rigid and the flexible ones with a slider mechanism. There is a trailing edge deflection of 2.5 mm for the small, rigid aerofoil and a trailing edge deflection of 4 mm for the small, flexible aerofoil with a slider mechanism attached to the loaer skin. A bigger size aerofoil is fabricated and the SMA wires are connected to the slider itself and this arrangement has given a trailing edge deflection of 17 mm.

Final configuration of the SMA wire integrated aerofoil is to be designed to achieve 15^0 trailing edge deflection. An active control system to actuate the SMA wire is to be developed. The ultimate objective of this project is to demonstrate a morphing aerofoil structure in a low speed (10-50 m/s) wind tunnel test. The success of the proposed design and the subsequent tests should be quantified in terms of the controllable variation in the aerodynamic coefficients under steady flow with respect to thermo-electric energy input.

Bibliography

[1] C. Bauer, W. Martin, H.F. Seigling, H. Schurmann, "A new structural approach to variable camber wing technology of transport aircraft," AIAA-A98-25050.

[2] J.P. Florance, A.W. Burner, G.A. Fleming, C.A. Hunter, S.S. Graves, C.A. Martin, "Contribution of NASA Langley research center to the DARPA/AFRL/NASA/Northrop Grumman smart wing program," *AIIA-2003-1961, 4th AIAA/ASME/ASCE/AHS Structures, Structural Dynamics and Materials Conference*, April 7-19, 2003.

[3] J. Bowman, B. Sanders, T. Weisshaar, "Evaluating the impact of morphing technologieson aircraft performance," AIAA-2002-1631.

[4] Jason. B, Brian. S, Bryan. C, Jayanth. K and Shiv Joshi, Terrence Weisshaar, "Development of Next Generation morphing aircraft structures," *48th AIAA/ASME/ASCE/AHS/ASC Structures, Structural Dynamics, and Materials Conference* 23 - 26 April 2007, Honolulu, Hawaii.

[5] Jason C. Bowman, Ryan W. Plumley,Jeffrey A. Dubois, David M. Wright, "Mission effectiveness comparisons of morphing and non-morphing vehicles," *6th AIAA Aviation Technology, Integration and Operations Conference* (ATIO) 25 - 27 September 2006, Wichita, Kansas.

[6] A. Ko, L.T. Leifsson, J.A. Schetz, W.H. Mason, B. Grossman, R.T. Haftka, "Multidisciplinary design optimization of a blended-wing-body transport aircraft with

distributed propulsion," *AIAA 3rd Annual Aviation Technology Integration, and Operation (ATIO) Technical Forum*, Denver, CO 17-19 Nov. 2003.

[7] M. Amprikidis, J.E. Cooper, O. Sensburg, "Experimental investigation of an all movable vertical tail model," *AIAA-2003-1413, 44th AIAA/ASME/ASCE/AHS structures, Structural Dynamics, and Materials Conference*, Norfolk, VA, April 7-10.

[8] D. Cadogan,T.Smith, R. Lee, S. Scarborough, D. Graziosi, "Inflatable and rigidizable wing components for unmanned aerial vehicles," *AIAA-2003-1801, 44th AIAA/ASME/ASCE/AHS structures, Structural Dynamics, and Materials Conference*, Norfolk, VA, April 7-10, 2003.

[9] D. Cadogan, T. Smith, F. Uhelsky, M. Mackusick, "Morphing inflatable wing development for compact package unmanned aerial vehicles," AIAA 2004-1807 SDM Adaptive structures forum.

[10] D. Cowan and G. Andersen, "Aeroelastic modelling, analysis and testing of morphing wing structures," *AIAA-2007-1734, 48th AIAA/ASME/ASCE/AHS/ASC structures, Structural Dynamics, and Materials Conference*, Honolulu, Hawaii, April 23-26, 2007.

[11] W. Shyy, M. Berg, D. Ljungqvist, "Flapping and flxible wings for biological and micro air vehicles," *Progress in Aerospace Sciences*, 35, 455-505, 1999.

[12] S. Ho, H. Nassef, N. Pornsinsirirak, Y.C. Tai, C.M. Ho, "Unsteady aerodynamics and flow control for flapping wing flyers," *Progress in Aerospace Sciences*, 39, 635-681, 2003.

[13] O.K. Rediniotis, L.N. Wilson, D.C. Lagoudas and M.M. Khan, "Development of a shape-memory-alloy actuated hydrofoil," *J. Intelligent Material Systems and Structures*, 13, 35-49, 2002.

[14] J.K. Strelec, D.C. Lagoudas, M.A. Khan and J. Yen, "Design and Implementation

of a shape memory actuated reconfigurable airfoil," *J. Intelligent Material Systems and Structures*, 14, 257-273, 2003.

[15] Whitting, Jan, Koray Safak and George G. Adams, "SMA Actuators applied to biomimetic underwater robots," Neurotechnology for Bibmimetic Robots. Ed.JOseph Avers, JOel L.Davis, and Alan Rudolph. The MIT Press:Cambridge, MA,2002.

[16] Rediniotis, Othon K and Dimitris C. Lagoudas, " Shape Memory Alloy Actuator as Locomotor Muscles," AIAA,2001.

[17] Kudva J.N, K. Appa, A. Jardine, C. Martin and B. Carpenter, "Overview of Recent Progress on the DARPA/USAF Wright Laboratory'Smart MAterials and Structures Development-Smart Wing' Program," *SPIE* Vol.3044,1997.

[18] Jardine, Peter, John Flanigan, Chris MArtin, and B. Carpenter, "Smart Wing Shape Memory Alloy Actuator Design and Performance," *SPIE* Vol.3044,1997.

[19] Liang, Jia and Rogers, "Behaviour of Shape Memory Alloy Reinforced Composite Plates PartII:Results," *Proceedings of the 30th Structures, SDM Conference*, AIAA-89-1331 CP, pp 1504-1513, 1989.

[20] Rogers C.A, "Active Vibration and Structural acoustic control of Shape Memory Alloy Hybrid Composites:Experimental Results," *Journal of Acoustical Society of America*, 88(6): 2803-2811,1910.

[21] Baz, Imam, and McCoy, "Active Vibration Control of Flexible Beams Using Shape Memory Actuators," *Journal of Sound and Vibration*, 140(30): 437-456, 1910.

[22] Bidaux J, J. Mansion, R. Gotthardt, "Active Stiffening of Composite Materials by Embedded Shape Memory Alloy Fibres," *Materials Research Society Proceedings*, 459(1997):107.

[23] Balta J.A, V. Michaud, M. Parlinska, R. Gotthardt and J. Mansion, "Adaptive Composites with Embedded NiTiCu Wires," *Proceedings of SPIE: Smart Structures and Materials 2001: Active Materials: Behaviour and Mechanics*. Vol.4333,2001.

[24] White S.R, M.E. Whitlock, J.B. Ditman and D.A Hebda, "Manufacturing of adaptive Graphite/Epoxy Strucutres with Embedded Nitinol Wires," *Adaptive Structures and Material Systems*- ASME. AD vol.35.ASME, New York, 1993.

[25] Hebda D.A, M.E Whitlock, J.B Ditman and S.R White,"Manufacturing of adaptive Graphite/Epoxy Strucutres with Embedded Nitinol Wires," *Journal of Intelligent Materials Systems and Structures*. Vol. 6, March 1995.

[26] Hebda D.A, S.R White, " Structural Behaviour of Composite Beams," *Adaptive Material Systems* AMD Vol.206/MD Vol. 58, 1995.

[27] Song G, B. Kelly, B.N Agarwal, P.C Lam and T.S Srivatsan, "Application of Shape Memory Alloy Wire Actuator for Precision Position Control of a Composite Beam," *Journal of Materials Engineering and Performance* Vol.9(3), June 2000.

[28] Cezar GD, Paul MW, Filippo M. Concepts for morphing airfoil sections using bi-stable laminated composite structures. *Thin-Walled Structures* 46 (2008) 689701.

[29] Edward AB, Benjamin KSW, Curt SK, Norman MW. Design and Fabrication of a Passive 1-D Morphing Aircraft Skin. 49th AIAA/ASME/ASCE/AHS/ASC Structures, Structural Dynamics, and Materials Conference,7 - 10 April 2008, Schaumburg, IL.

[30] W.T. Duerig, N.K. Melton, D. Stockel, M.C. Wayman, "Engineering Aspects of Shape Memory Alloys," Butterworth-Heinemann, London, Boston MA, 1990.

[31] V. Birman, "Review of mechanics of shape memory alloy structures,"*Appl. Mech. Rev*, **50**, pp. 629-645, 1997.

[32] J.A. Shaw, S. Kyriakides, "Thermomechanical aspects of niti," *J. Mech. Phy. Solids*,**43**(8), pp. 1243-1281, 1995.

[33] D. Bernardini, T.J. Pence, "Shape memory materials, modeling," In: *Encyclopedia of Smart Materials, John Wiley & Sons*, pp. 964-980, 2002.

[34] A.F. Devonshire, "Theory of ferroelectrics," *Adv. Phys* **3**, pp. 86-130, 1954.

[35] I. Muller, S. Seelecke, "Thermodynamic aspects of shape memory alloys," *Math. Comput. Model*, **34**, pp. 1307-1355, 2001.

[36] C. Friend, "Shape memory alloys," *In: Encyclopedia of Materials, Science and Technology, Elsevier Science*, pp. 1-7, 2001.

[37] E. Graesser, F. Cozzarelli, "Shape memory alloys as new materials for aseismic isolation," *J. Eng. Mater*, **117**, pp. 2590-2608, 1991.

[38] S. Zhang, G.P. McCormick, "Thermodynamic analysis of shape memory phenomena - i. Effect of transformation plasticity on elastic strain energy," *Acta Mater*, **48**, 3081-3089, 2000a.

[39] L. Delaey," Diffusionless transformations, In: Cahn, R.W., Haasen, P., Kramen, E.J. (Eds.), Phase Transformations in Materials," *Material Science and Technologies*, **5**. VCH Publishers, New York, pp. 339-404 (Chapter 6), 1990.

[40] H. Tong, C. Wayman, "Characteristic temperatures and other properties of thermoelastic martensites," *Acta Metall*, **22**, pp. 887-896, 1974.

[41] K. Otsuka, C.M. Wayman, "Introduction, In: Shape Memory Materials," *Cambridge University Press*, Cambridge, pp. 1-26, 1999.

[42] Z. Nishiyama, "Martensitic Transformations," *Academic Press*, San Diego, 1978.

[43] L. Kaufman, Cohen, M., "Martensitic transformations. In: Chalmers, B., King, R. (Eds.)," *Progress in Metal Physics*, **7**, Pergamon Press, Oxford, pp. 165-246, 1958.

[44] J. De Vos, E. Aernoudt, L. Delaey, "The crystallography of the martensitic transformation of BCC into 9R: a generalized mathematical model," Z. Metallkde **69**(H7), pp. 438-444, 1978.

[45] T. Saburi, C.M. Wayman, K. Takata, S. Nenno, "The shape memory mechanism in 18R martensitic alloys," *Acta Metall*, **28**, pp. 15-32, 1980.

[46] Brinson, L.C., 1993. One dimensional constitutive behavior of shape memory alloys: thermomechanical derivation with non-constant material functions and redefined martensite internal variable. J. Intell. Mater. Syst. Struct. 4 (2), 229-242.

[47] V.R. Buravalla , A. Khandelwal, "Differential and integrated form consistency in 1-D phenomenological models for shape memory alloy constitutive behaviour," International Journal of Solids and Structures 44 (2007) 4369-4381.

[48] E.L. Houghton, P.W. Carpenter, "Aerodynamics for engineering students", Fourth edition, Edward Arnold press.